Intelligent Power Grasp Through Layered Magnetization by A Serial Arm Field Robot

Debanik Roy*

Board of Research in Nuclear Sciences, Department of Atomic Energy, India

Abstract: Field applications of serial-arm static robotic system for material handling operations pose serious technological challenges under *unstructured* environments, in contrast to the same in situations with *known* perspectives of the obstacles therein. The present paper describes the design, analysis and development of a novel *magnetic gripper*, along with its sensorized *peripherals*, deployed in a non-coherent unstructured workspace. The prototype gripper was augmented with a four degrees-of-freedom SCARA type industrial robot and the field-unit was programmed to perform the intended operation of handling steel bearing races of various categories round-the-clock. The robotic cell was equipped with multiple sensors, hardware interfaces and safety measures (e.g. electronic light barrier), designed indigenously. The paper also analyses the performance of the magnetic gripper in the *field* through mathematical model, pertaining to this maiden application of robotics in Indian steel industries.

Keywords: Field robot, unstructured environment, magnetic gripper, power grasp, bearing ring, industrial robot, robotized handling, sensory system.

1. INTRODUCTION

A customized industrial application of robotic system in an *unstructured environment* is recognized to be more pragmatic compared to applications under *structured layouts*. Augmentation of a tailor-made gripper with the field manipulator, interfaced with multiple sensory systems, has attenuated the technological up-gradation so far as industrial application of robots are concerned. The present paper delineates the developmental details of a novel magnetic gripper-based *robotic cell*, which was commissioned in the shop-floor of *Tata Steel*, India. The SCARA type robotic system, equipped with this prototype magnetic gripper, performs the tedious material handling operation of unloading and loading of steel bearing races round-the-clock. The *wrist* force sensor, fitted with the magnetic gripper, is used to sense the *load* coming on the manipulator during the loading / unloading operation is in progress. The paper also postulates characteristic model related to the gripping action of the said gripper, based on finite element analysis (FEA). The results on the field-trials of the developed gripper are also described with analysis. Besides, the paper focuses on an analytical solution for the activation of the gripper system, through *micro-motion path* planning. It may be mentioned that *magnetic gripping* is still an *open* research problem in robotics and whatever applications of magnetic grasp, reported earlier, were either with very low payload or intended for structured environment.

In recent past, several researchers have studied the aspects of magnetic field effect on the substrate and its associated characteristics, such as *resilience*. A survey of available literature in this regard highlights on the theoretical models concerning the physics of magnetism. Characteristic attributes of the magnetic materials with respect to their field intensity have been reported through the postulation of a complete–moving hysteresis model [1, 2]. Besides, finite element solution of periodic steady state magnetic field problems in soft materials with scalar hysteresis was analyzed [3]. The authors have used *Jiles - Atherton model* for the generation of symmetric B-H loops and it has been coupled with the *Fixed Point Technique* for handling magnetic non-linearities. In fact, majority of the archived models on magnetic hysteresis, e.g. Preisach model and the Jiles-Atherton model, are generally H-based (forward) and thereby unsuitable for modeling hysteresis when augmented with the B-oriented FEA equations, as the models need to be inverted [4, 5]. However, sidetracking the issue of *forward* (H-based) vis-à-vis *inverted* (B-based) models, the paradigm of magnetic pull variation under an unstructured environment of materials and the residual magnetism in such a situation were not discussed in none of the above citations, which is, a vital aspect so far as the application modality of the present robotic unit is concerned.

Over the years, the finite element method (FEM) has evolved as a useful tool by choice towards calculating the magnetic field-strength (static), where other analytical or model-based methods cannot be used because of geometrical complexities as well as

*Address correspondence to this author at the Board of Research in Nuclear Sciences, Department of Atomic Energy, India; Tel: 0091-22-25593946; Fax: 0091-22-25505151; E-mail: deroy@barc.gov.in

E-ISSN: 2409-9694/15

non-linear properties of the magnetic material. For example, magnetic analysis using a two-dimensional FEM was performed with reference to non-linear hysteric materials [6] vis-à-vis ferromagnetic materials [7]. Nonetheless, structural anomalies in the magnet design are identified through FEM [8] and deflection patterns under magnetic loading are noted [9, 10]. Besides, the modalities of the FEM software packages were re-tuned for spatial harmonic analysis of the unshielded magnetic field [11] as well as three-dimensional linear and non-linear magnetic field problems [12, 13]. A new semantic was proposed using FEM towards comprehending the analysis for tangentially continuous 3D edge elements, such as tetrahedral and hexahedral elements, using *symbolic algebra*, where in we get a much faster convergence rate [14]. Likewise, discrete finite formulation may well be inducted in situations of unstructured finite element (FE) meshes, either in plane or in space, in order to obtain fourth-order convergence [15] or even for discrete *patterned* media [16] and coupled time-stepping FEA in accessing dynamic performance of magnetic assembly [17].

Fast computation of linear equation-sets of the FEM matrices is an important pre-condition for evaluating magnetic field-strength, especially in unstructured environments. Besides tailor-made *optimization* techniques [18, 19], algebraic multigrid methods (AMG) are efficient linear solvers in this regard, utilizing nodal and edge elements [20]. Nonetheless, computations can be made even faster by augmenting domain decomposition method (DDM) to AMG, both nested in the common FEM module, culminating in better convergence [21]. Customized algorithm was also invoked for the analysis of *periodic* structures, such as our design of the *elemental magnets*, using non-matching triangulation of the FE mesh [22].

A sandwich treatment of FEM and BEM (boundary element method) has also been tried for the analysis of magnetic field strength using 3D linear elements [23] vis-à-vis adaptive mesh less method (MLM), which uses scatter nodes and detours traditional FEM-mesh structure with explicit element-geometry [24]. Model-based approach towards estimating the error in computing magnetic force inside a static field is used too, which is at times becomes as significant as the discretization error [25]. The principle of virtual work has been adopted in computing magnetic field-strength, based on FE mesh of the magnetic substance [26].

It may be noted that all of these researches related to hysteresis (B-H) curve, cited above, were based on uniform magnetic field (H) consideration. But, in our case, the magnetic field is highly non-uniform because of the haphazard placement and subsequent layout of the bearing rings. And, since the magnetic field itself is non-uniform, we can't apply standard models (e.g. Jiles-Atherton model) to this case; rather we need to depend on improvised design, which will have higher level of field-density (B). Our design of the magnetic gripper incorporates various *cell-magnets*, which counters the non-uniformity in magnetic field intensity and imbibes higher field-density by induction.

Apart from the analysis of the magnetic field, issues like integration and propagation of geometric sensor observation and active sensory processing in a *field robotized system* has been addressed by the researchers [27-29]. Nonetheless, miscellaneous facets of multi-sensory data fusion for a robotic system, including logical specifications, have also been reported [30, 31]. However, barring theoretical aspects, a real-time sensor fusion model essentially demands for [a] strategy for *centralized estimation* [32]; [b] adoption of optimal *fusion method(s)* [33, 34] and [c] *localization of the fused data* [35]. In-line with our field application, a stochastic model was developed for robotized assembly operation using multiple sensors, viz. force/ torque, proximity and laser sensor [36, 37]. Also, a detailed system layout vis-à-vis modeling of a multi-sensory system was presented for handling steel bearing races in an unstructured industrial environment [38]. The uniqueness of this magnetic grasp in shop-floor condition was described with reference to results on the commissioning trials, with detailed modeling and parametric analysis of the ring-grasping phenomenon [39].

The paper has been organized in six sections. Section 2 describes the features of the robotic system, with details regarding workspace layout, sensory models and interfacing with the gripper unit. A detailed description on the design and construction of the magnetic gripper, along with characteristic functional paradigms, based on real-life performance testing is reported in section 3. The logistics, FEM modeling of the gripper and subsequent analysis of the simulated results have been addressed in section 4. Section 5 delineates the modeling, performance evaluation and test results of the gripper system at the shop-floor and finally, section 6 concludes the paper.

2. DESCRIPTION OF THE FIELD ROBOTIC SYSTEM

2.1. Layout of the Robotic Workspace and Process

The four degrees-of-freedom SCARA robot (Make: *Staubli Unimation Inc*, *U.K.*, Model: RS 154-22-CS3), having 60 kg payload capacity was installed for unloading and loading of steel bearing rings using the custom-built magnetic gripper. The robot has got one translatory joint having vertical stroke of 2.2metres, while other three joints are revolute type, with a horizontal reach of 1.5metres. Figure **1** shows the overall structure of the robotic manipulator, as commissioned in the shop-floor.[1]

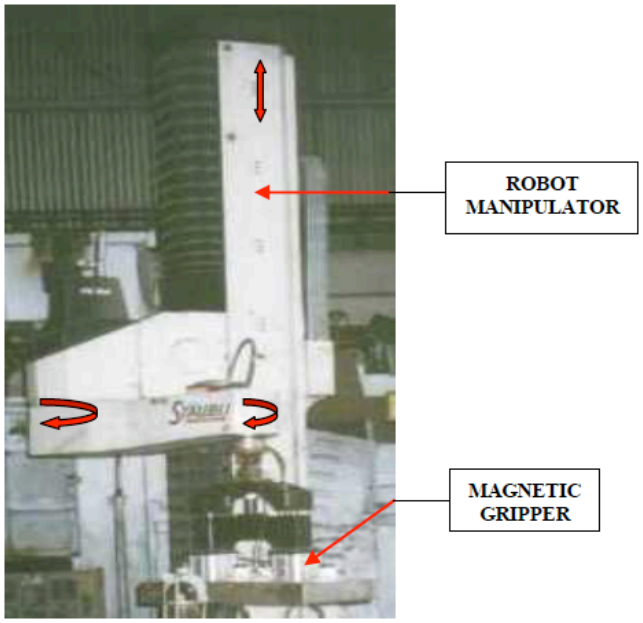

Figure 1: Photographic View of the Robotic System Commissioned.

Rings are required to be loaded from large-sized loading bins to small-sized baskets, moving on a conveyor. After getting annealed inside the furnace, those are to be unloaded from the baskets to a separate unloading bin. Each basket can accommodate approximately 250kg. of rings, assuming a combination of different types and/or sizes (Roy, 2005). The robot has been installed in the vicinity of the continuous annealing furnace, so that the planar work-envelope of the robot can cover-up the bins, baskets as well as specific conveyor locations (i.e. locations wherefrom the baskets will be either pushed inside the furnace or halted for getting unloaded). The pusher mechanism of the main conveyor system helps the movement of the baskets to/from the furnace, respectively at the beginning and ending of the heat treatment cycle. The robotic system has been interfaced with three different types of sensors, namely, a force sensor (placed over the gripper), an array of infrared sensors (for *light barrier*), a touch-type part sensor (for detecting the locations of bins / baskets) and a pair of special contact-type part sensor (for detecting the *park position* of the robot). Figure **2** shows the photographic view of the robotic cell in the shop-floor.

Figure **3** shows the schematic layout of the robot workspace in two dimensions. As detailed in Figure **2**, the field consists of two proximity sensors (one each for LB and UB), one part sensor, one load cell and 16 nos. infrared sensors (8 pairs of emitters and detectors; branched out in 4 nos. each on four ELB-pillars). Layout-wise, *zone 1* (Ω_1) contains a total of 9 sensors (proximity sensor 'F' and 8 nos. infrared sensors, 'J'); while *zone 2* (Ω_2) has 2 sensors ('H' and 'I') and *zone 3* (Ω_3) has 9 sensors in total ('G' and 8 nos. 'J').

2.2. Sensory System Layout and Models

2.2.1. Force Sensor (Load Cell)

The force sensor, in the form of a *load cell*, mounted on the wrist of the SCARA robot and fitted with the magnetic gripper, is used to sense the vertical force ('load') coming on the manipulator while the loading / unloading operation of the rings is in progress. The sensor is capable of generating the output against the force sensed, viz., F_z, through its built-in microprocessor in user-selectable units, at a particular time-instant. The sensor works on the principle of strain gauge *Wheatstone bridge*. It is also equipped with a display unit, which can be programmed and edited suitably by the user. This digital display unit shows the amount of rings handled for each of the robotic cycles, in kg. vis-à-vis the 'overload' condition, i.e. when the rings inside the bin or the basket obstruct the gripper. This overload condition signifies a heavy compressive load on the gripper above its payload capacity and is manifested in the display unit with a minus sign at the beginning and followed by a digital number (kg. value). The microprocessor management of the indicator unit allows easy setting up and calibration of the unit. All the trip limit and calibration data are retained in a non-volatile memory and alteration of the data is password protected. It has a +/- 15 bit A/D converter, taking many readings per display update and the number of averaged readings (by digital filtering) is user-

[1] Apart from the two revolute joints labeled in Figure **1**, the robot has a rotary base joint too, which is not shown in the figure.

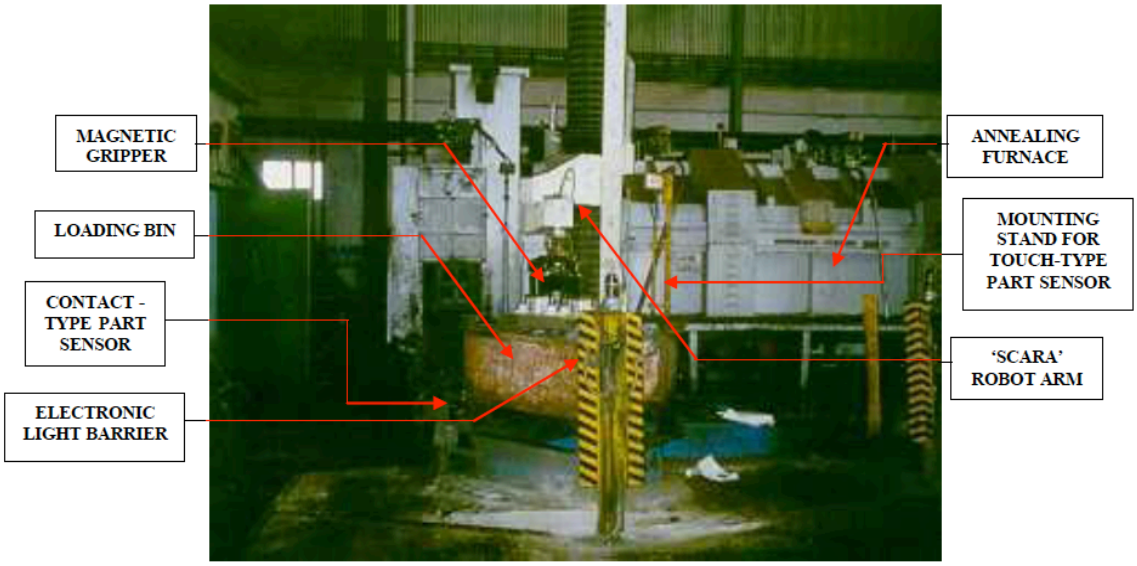

Figure 2: Photographic View of the Robotic Work-cell at the Shop-floor.

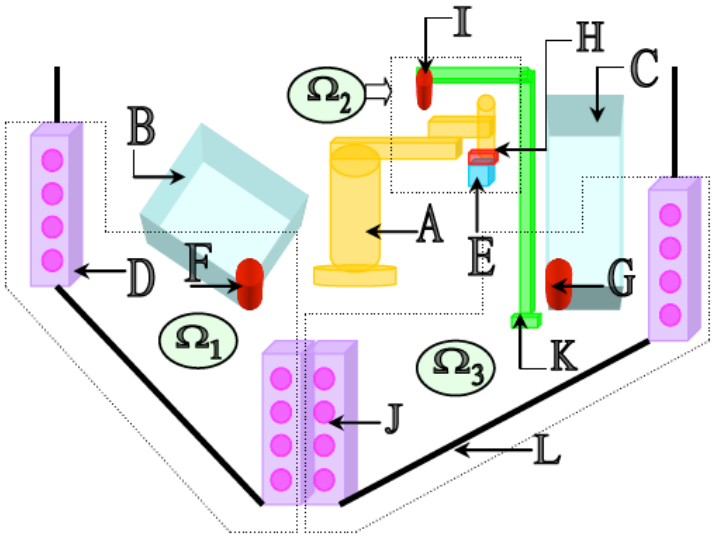

Index: A: Industrial robot; B: Loading bin (LB); C: Unloading bin (UB); D: Electronic light barriers (ELB) [4 nos.]; E: Magnetic gripper; F: Proximity sensor for LB; G: Proximity sensor for UB; H: Load cell; I: Part sensor for robot's 'home'; J: Infrared sensors; K: Stand to house 'I'; L: Near-actual physical boundary of the robotic workspace; Ω_1, Ω_2 and Ω_3: Sensory zones.

Figure 3: Schematic Layout of the Robot Workspace in Two Dimensions.

selectable over a wide range. The instrument is equipped with five *boards*, respectively for current input, analog output, fast maximum / minimum output, replay output and serial communication.

The current input board is for use with any transducer with a 0 to 20mA or 4 to 20mA current output and requiring either a + 15 volts (ground referenced) or 24 volts (non-isolated) excitation. Analog output board provides two outputs, viz. a voltage output ranging upto +/- 10V at 20mA and a separate current output providing the said current range into 0 to 470 ohms load(s). Fast maximum / minimum board is designed for use in dynamic application for which software-based standard max/min detect or response speed is too slow. This board allows full-scale signals having pulse widths or rise rates of as small as 1msec. To be monitored with accuracy purely dependent on the bandwidth characteristics of the input board. The instrument has got two opto-isolated RS 232C ports for serial communication. The transmit / receive interface has a fixed data rate of 9600 baud, while the line printer interface has a selectable baud rate from 110 to 9600.

The output from the force sensor, ψ_{fs} (t), has been modeled as:

$$\begin{aligned}\psi_{fs}(t) &= -\xi, \quad \forall t_j \neq t_{i,} \qquad t_j \in T, \quad j \neq i \\ &= \Phi(t_i), \quad \forall t_{i,} \quad \sum_{i=1}^{i=n} t_i \leq T\end{aligned} \tag{1}$$

Where, T: Total time-period during which the magnetic gripper is activated (i.e. the robotic cycle is in progress); t_j: $j^{th.}$ time-instant, during which *overload* condition occurs; t_i: $i^{th.}$ time-instant, during which permissible load is being pulled up by the gripper and n: Total number of *successful picks* by the gripper.

It is to be noted that,

$$\sum_i t_i + \sum_j t_j = T \tag{2}$$

The output from this force sensor is tangible while the gripper is pulling up permissible load, viz. Φ (t_i), while ξ signifies the digital sensory display as and when overload condition occurs, either during unloading or loading cycle. Overload condition occurs when the gripper attempts to pick excessive load and that very pick is being released off immediately to avoid eventual damage to the sensor and robot system, in general. Nonetheless, the load cell remains activated as long as the magnetic gripper is powered ON, i.e. while the robotic cycle is in progress. The overload situation may arise due to either of the two reasons, namely: [i] if the gripper tries to pull rings, weighing more than the payload capacity of the same at that operating speed and [ii] if the gripper suddenly hits the heap of the rings by giving a 'jerk'. The above two conditions have been studied analytically and the conclusions drawn there from are:

i if $|\xi| >> W_G$, where W_G is the payload capacity of the gripper, in the limiting condition, we have,

$$Lim_{\delta \to 0} \Psi_{fs}(t) = \Phi(t_i) \tag{3}$$

Where, $\delta = |\xi - W_G|$

ii In case of jerk, which essentially occurs due to jamming of rings in a haphazard manner inside the bin and/or basket, the gripper tries to push the rings by exerting a large amount of compressive force in comparison to its payload capacity. Essentially, it signifies an *impulse* on the gripper, which acts for an infinitesimal time-period during which overload condition prevails and the situation gets manifested with a large *tilt* of the gripper over the heap of the rings (refer Figure **4**). Mathematically, it signifies,

$$Lim_{\Delta t_i \to \varepsilon} \Psi_{fs}(t) = \infty \tag{4}$$

Where, $|\varepsilon| \to 0$ and Δt_j is the $j^{th.}$ infinitesimal time-period during which overload condition prevails. Essentially, it signifies an impulse on the gripper, which culminates in the following expression, viz.

$$\int_{t=0}^{t=\Delta t} \Psi_{fs}(t)\, dt = \left|\xi(\Delta t_j)\right| \tag{5}$$

Figure 4: The Tilt of the Magnetic Gripper Facing Jerk During Grasping.

It is to be noted that $\Phi(t_i)$ is a complex conjugate form of the load cell data, which is influenced directly by the five parameters, viz. [a] number of rings gripped (n_r); [b] average size of the rings gripped (d_r); [c] orientation of the rings (φ_r), i.e. whether gripped horizontally or vertically; [d] number of layers produced (l_i) and [e] zonal attribute of the magnetic pull (λ_r), which essentially depends on the average inclination of the *heap* at a particular time-instant. However, it is not possible to have any sort of mathematical expression for $\Phi(t_i)$ as a function of the above parameters, because of the inherent randomness of the very process. Among these parameters, the load cell output at a particular time-instant, say $\psi_{fs}(t)$, has got somewhat direct proportional relationship with n_r, l_j and d_r . As a matter of fact, repeated field-trials have revealed that ψ_{fs} (t) varies exponentially against these three parameters. However, the trend is reverse for the heap inclination, λ_r. So far as the variation of ψ_{fs} (t) with φ_r is concerned, no stable relationship was observed,

although lesser lifts by the gripper were confirmed whenever the *relative* angular orientation[2] of the rings placed were comparatively *large* enough.

Based on the field-run results, empirical relationships between the load cell output, i.e. $\Phi(t_i)$ and the three parameters, namely n_r, d_r and l_j have been established. These are as follows,

$$\Phi(t_i) = K_1 e^{n_r}; \quad \Phi(t_i) = K_2 e^{d_r}; \quad \Phi(t_i) = K_3 e^{l_i} \tag{6}$$

Where, K_1, K_2 and K_3 are suitable numerical constants, not related concurrently. Thus, we can formulate a conjunctive relationship for $\Phi(t_i)$ out of the above three sub-expressions as,

$$\Phi(t_i) = \frac{K_1 e^{n_r} + K_2 e^{d_r} + K_3 e^{l_i}}{3} \tag{7}$$

Unlike the above-mentioned three parameters, it has been verified from experimentation that the variation of load cell output with respect to λ_r at any time-instant, t_i can be mathematically expressed by the following equation, viz.,

$$\Phi(t_i) = -m\lambda_r(t_i) + \Phi_0\Big|_{at\ t=t_i} \tag{8}$$

Where, $\Phi(t_i)$ is the load cell data at any time-instant t_i during which the gripper performs a 'positive' lift and 'm' is the slope of the regression line. The heap inclination, λ_r is also a time-dependent variable here and its value will get changed from one instant to another during successful picks. The parameter, Φ_0 is a constant at $t=t_i$, but it is a function of K_1, K_2 and K_3. Although equation (8) is a simplified analogy of the exact real-time situation, it can be accepted as a potential approximation.

The randomness of the sensory output has been modeled by considering the probability density function (p.d.f.) of it, based on the

Gaussian distribution. This particular p.d.f. was selected because of better transducer stabilization, good environmental handshaking and repetitiveness of the operation involved. The distribution is given by,

$$P_{lc}(X^i_{lc}, t_i) = \frac{1}{\sqrt{2\pi}\sigma_{lc}} \exp\left[-\left(X^i_{lc} - \mu_{lc}\cdot\lambda_r\Big|_{at\ t=t_i}\right)^2 \Big/ 2\sigma^2_{lc}\right], \forall t \in I \tag{9}$$

[2] This means the angular difference (say, in degrees) in positioning one ring with respect to the rings surrounding it.

Where, P_{lc} (X_{lc}, t_i): Probability associated with the acquisition of sensory data at the load cell at $i^{th.}$ time-instant; X^i_{lc}: Observation (i.e. sensor data) at the $i^{th.}$ time-instant; μ_{lc}: Mean of the observations; σ^2_{lc}: Variance of the observations; $\lambda_{r|t=ti}$: Heap inclination at $i^{th.}$ time-instant.

2.2.2. Part Sensors

Two different types of *part sensors* were used in the robotic cell, viz. a] *contact-type* (for detecting the location of the bin) and b] *touch-type* (for detecting robot's *home* position). The sensors purely work on the basis of ON-OFF signal, i.e. the sensors generate a specified voltage signal when the terminal activity (e.g. reaching robot's home position or detecting the bins) is over.

Contact-type part sensors (limit switch) were placed at one corner of the bin(s), amongst the four such available for both loading and unloading bins (refer Figure **2**). The sensors verify the presence or absence of the respective bins in place, in order to initiate the robotic cycle. Thus, symbolically the output of the contact-type part sensor can be modeled as,

$$\begin{aligned} &\psi^c_{ps}(t) = 0, \quad \forall t = t_m \\ &= K^c_{ps}, \quad \forall t = t_n \qquad m \neq n \end{aligned} \tag{10}$$

Where, $\psi^c_{ps}(t)$: Sensory output (in milli-volts) at the $t^{th.}$ time-instant; t_m: $m^{th.}$ time-instant, when the bins are not in position (i.e. the robotic cycle is not in operation); t_n: $n^{th.}$ time-instant, when the bins are in proper position, in course of the robotic cycle in progress.

A touch-type part sensor was also provided in the system to check the exact *parking* (home) position of the robot at the end of each cycle. The activation of this sensor was manifested by the situation when the magnetic gripper *touches* it and consequently, the sensor produces zero voltage reading while the robotic cycle is in operation. The sensor was mounted on a long vertical stand; beside the conveyor track and in front of the annealing furnace (refer Figure **2**). This sensor was interfaced with the pair of sensors for position checking of the bins. Thus, the output of the touch-type part sensor can be modeled as,

$$\begin{aligned} &\psi^t_{ps}(t) = 0, \quad \forall t = t_i \\ &= K^t_{ps}, \quad \forall t = t_j \qquad i \neq j \end{aligned} \tag{11}$$

Where, $\psi^t_{ps}(t)$: Sensory output (in milli-volts) at the $t^{th.}$ time-instant; t_i: $i^{th.}$ time-instant, when the robotic cycle is

in operation; t_j: $j^{th.}$ time-instant, when the robot reaches the *park* position.

Because of the discrete and binary nature of the output, the stochastic model for these sensors has been formulated considering Binomial distribution as the probability mass function (p.m.f.), i.e.

$$P^{k}_{ps}(x,t) = {}^{n}C_{x}(p)^{x}(1-p)^{n-x} \qquad \forall k = 'c' \ \ or \ \ 't' \tag{12}$$

Where, P^{k}_{ps} (x, t): Probability of having sensory output at the $t^{th.}$ time-instant; n: Total number of observations made; x: Measured variable, i.e. the distance between the sensor and the object surface; p: Probability of *success*, i.e. *part* is detected, meaning either the bins are in position (in case of contact-type sensors) or the robot has reached its *park* position (in case of touch-type sensor).

It may be commented that the most crucial aspect of the evaluation of P^{k}_{ps} (x, t) lies with the perfectness of determining 'x'. Mathematically, we can infer the interpretation of 'x' as,

$$x = \lim_{\xi \to 0} \{ d_{ob}(\xi) - \xi \} \tag{13}$$

Where, ξ: The *desired* distance between the sensor and object (plane) and $d_{ob}(\xi)$: The *observed* distance between the sensor and object, as a function of desired distance.

2.2.3. Infrared Sensors

The robotic system is made operative with the help of an indigenously designed light barrier, pentagonal in shape, activated through an array of 12 nos. infrared sensors. The sensors, made of NPN type semiconductor with *normally open* ('NO') type contacts, work on the principle of infrared radiation as generated by separately placed emitters and detectors, acting as pairs. The sensing range and intensity of infrared radiation can be controlled manually as the system demands. All of these sensors have been duly calibrated before testing for performance. The calibration results support linearity and are in good agreement with the theoretical values. The central pillar (amongst the total five) of the said system consists of two boxes, having detector sensors, 3 nos. each, and the corresponding emitters are located on the right-hand side and left-hand side pillars [Roy, 1997]. The remaining pillar is a dummy one, in the sense that it only provides physical guarding. The controller system is equipped with a D.C. power supply unit (10-30V variable), miscellaneous junction connectors, jumpers and cables and a converter card (on PCB) to provide a single analog output out of six nos. detectors. The final output goes to the I/O port of the robot controller through electrical relay.

These sensors work on the range-finding principle within their permissible zone of operation and culminate in analog output, similar to binary form. In other words, the light barrier produces a high voltage as and when the barrier is broken, due to the penetration of the object(s); else, it will generate zero voltage. Mathematically, the paradigm can be modeled as,

$$\begin{aligned} \psi_{ir}(t) &= 0, \quad \forall t = t_p \\ &= K_{ir}, \quad \forall t = t_q \qquad p \neq q \end{aligned} \tag{14}$$

Where, ψ_{ir} (t): Sensory output from the pair in volts at the $t^{th.}$ time-instant; t_p: $p^{th.}$ time-instant, when the light barrier is not obstructed; t_q: $q^{th.}$ time-instant, when at least one object gets inside the guarding system.

The system works on the principle of discrete output over an infinite time-period and culminates in a p.d.f. following Poisson distribution. The distribution is given by,

$$P_{ir}(y,t) = \frac{\exp^{-\lambda} \lambda^{y}}{y!}, \qquad \forall \quad y = 0,1,2...,\infty \tag{15}$$

Where, P_{ir} (y,t): Probability of having broken barrier at $t^{th.}$ time-instant; y(t): Instantaneous distance of the penetrating object from the emitter; y: Observation at the $t^{th.}$ time-instant, where $0 \leq y(t) \leq y_{max,}$ where y_{max} is the maximum permissible distance between the emitter and detector pair and λ: Mean of the observations made, i.e. $\lambda = np(1-p)$, where 'n' is the total number of observations made and 'p' is the probability of *success*, i.e. the light barrier is broken.

2.3. Sensor Fusion and Reliability Analysis

2.3.1. Models for Sensor Data Fusion

Sensor fusion plays a vital role in the successful performance of the entire field robotic system. Two different fusion models, namely, multiplicative and additive, have been postulated to suit the real-life situation of this quaternary sensor system. The multiplicative model essentially deals with the multiplicative measure of the respective probability mass functions, while the additive model sums the

same. All of these sensors have been given equal importance so far as the measurement of a particular parameter is concerned. However, measurement signifies either quantitative (e.g. force sensor) or qualitative (e.g. infrared and part sensors) type.

The fusion models are expressed mathematically as,

$$P_{sys}(t) = \prod_{i=1}^{i=3} \eta_i P_m(t), \quad 0 \le \eta_i \le 1 \tag{16a}$$

and,

$$P_{sys}(t) = \sum_{i=1}^{i=3} \eta_i P_m(t), \quad 0 \le \eta_i \le 1 \tag{16b}$$

Where, $P_{sys}(t)$: System probability at $t^{th.}$ time-instant; η_i: Weightage factor for the $i^{th.}$ sensor, $\forall i=1,2,3$; $P_m(t)$: Individual probability measure, e.g. for the force sensor, part sensors and infrared sensor.

Optimization of the fused sensory data is an important aspect related to the performance study of the robotic system. This multi-sensory system being purely heterogeneous, measuring different parameters at a specific time-instant, cannot be tested for optimization by the standard procedures. However, assuming equal variance of all the four sensory measurements, we get,

$$\sigma_{lc}^2 = \lambda = np(1-p) \equiv \sigma^{*2} \tag{17}$$

Where, σ^{*2} denotes the homogeneous variance.

In order to minimize the variability between sensor data, $P_{sys}(t)$, corresponding to equations 16a and 16b, is to be differentiated with respect to σ^{*2}, which finally results in transcendental equations, viz. for the multiplicative model as per equation 16a, we have,

$$x(t) = \mu t + \sqrt{\left\{\frac{\sigma^{*2}}{2} + \sigma^{*4}\left(1 - 2\ln\sigma^*\right)\right\}} \tag{18}$$

And, for the additive model as per equation 16b, we get,

$$2\exp\left(-\sigma^{*2}\right)\sigma^{*2(x+2)}\left(2\ln\sigma^* - 1\right) + \exp\left\{\frac{-(x-\mu t)^2}{\sigma^{*2}}\right\} x!\left\{2\left(x-\mu t\right)^2 - \sigma^{*2}\right\} = 0 \tag{19}$$

Where, x(t) denotes the sensory data at the $t^{th.}$ time-instant during which the condition of *minimum variance* occurs.

On scrutinizing this *field* layout, we can study the nature of the variation of the *inter-sensor distance* (D_i) with the number of unit-sensors (N_p), in a generic form, as depicted in Figure **5**.

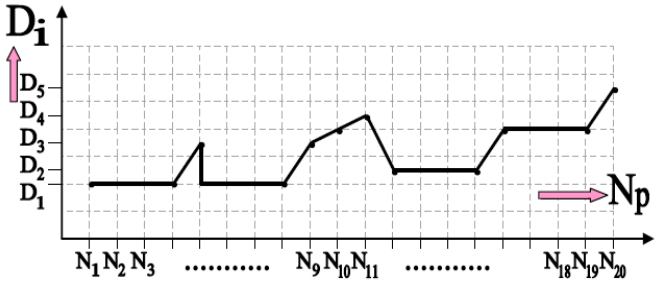

Index: $N_1$to N_8 and N_{12} to N_{19}: Infrared sensors in zone1 and zone3 respectively; N_9 and N_{20}: Proximity sensors for LB and UB; N_{10}: Load cell; N_{11}: Part sensor.

Figure 5: Generic plot showing the parlance of sensor placement inside the field.

It may be noted that the plot shown above can be extrapolated for any number of field sensor-units, with varying positional attributes. Besides, this plot can be used to ascertain relative influence of unit-sensors over the neighboring ones. Since all the unit-sensors are located staggered here, it is not possible to regularize these under a defined analytical pattern, e.g. 2D matrix, as all of the inter-sensor distances are unequal. Continuity of unit-sensors needs to be maintained all through.

2.3.2 Reliability Analysis for the Sensory Members

The reliability aspect of the individual sensory members has been studied in order to obtain analytical expression for the overall system reliability. As all of these sensors are used in the field in round-the-clock operation, system reliability is a crucial aspect from the design standpoint. For example, the individual reliability for the force sensor and the touch-type part sensor must be adequate, as we are using these two sensors only one in number. Thus, MTBF (Mean Time to Failure) of these two categories of sensors should be very high, as we cannot afford any malfunction due to these two sensors amidst the robotic cycle. In contrast, the other two categories, namely the contact-type part sensors and infrared sensors do enjoy multiplicity in numbers and thereby having *stand-by* members. In other words, reliabilities of these two sensory systems are cumulative in nature and the robotic system at field will still be sustained even if minor malfunction crops in.

The infrared sensors have been accommodated inside the light barrier (refer Figure **2**) and it has been

developed in a pentagonal shape (refer Figure **3**). Considering each pillar of the light barrier houses equal number of emitters and detectors, as in the present application, the overall reliability of the light barrier system with 'n' no. of sensors in each pillar becomes,

$$R_{ir} = 1-(1-r)^{4n} \tag{20}$$

Where, R_{ir}: Overall reliability of the light barrier and r: Reliability of the individual sensor, assumed to be equal. However, in case of unequal distribution of sensors on the left-hand side and right-hand side pillars with 'n' and 'm' nos. of pairs respectively, the expression for the overall reliability becomes,

$$R_{ir} = 1-(1-r)^{2(m+n)} \tag{21}$$

The generalized expression for the overall reliability for a light barrier having 'k' no. of pillars with 'q' no. of open-ends devoid of electronic guarding arrangement[3] with n_1, n_2, n_3,……..,n_k no. of sensor-pairs on respective pillar is givesn by,

$$R_{ir} = 1-(1-r)^{2(n_1+n_2+n_3+.....+n_k)} \tag{22}$$

Which, on simplification gives,

$$R_{ir} = 1-(1-r)^{2(k-q)n} \tag{23}$$

Where, $n_1 = n_2 = n_3 = \ldots\ldots = n_k$

Similarly, the generalized expression for the reliability of the contact-type part sensors, meant for detecting the presence or absence of the loading /unloading bin becomes,

$$R^{c}_{ps} = 1-(1-R)^{k}, \quad \forall k = 2,3,4 \tag{24}$$

Where, R^{c}_{ps}: Overall reliability of the contact-type part sensor(s); R: Reliability of the individual sensor; k: No. of possible redundancies based on the quadruple structure of the bin.

Hence, the reliability of the entire field robotic system will be,

$$R_{sys}(t) = R_{ir}(t)\cdot R_{fs}(t)\cdot R^{t}_{ps}(t)\cdot\left[R^{c}_{ps}(t)\right]^{2} \tag{25}$$

Where, $R_{sys}(t)$: System reliability at the $t^{th.}$ time-instant; $R_{fs}(t)$: Reliability of the force sensor at $t^{th.}$ time-instant and $R_{ps}^{t}(t)$: Reliability of the touch-type part sensor at $t^{th.}$ time-instant.

3. DESIGN AND DEVELOPMENT OF THE MAGNETIC GRIPPER

3.1. Magnetic Grasp Versus Other Alternatives

Grasping under unstructured environment is technologically challenging and involves a variety of *coherent contacts* between the *objects* to be gripped and the *gripper body*. The first and foremost consideration for conceptualizing an ideal grasp is associated with the type of object(s) to be grasped. In the present situation, the graspable objects, viz. steel bearing races; being ferromagnetic, the default choice becomes a magnetic gripper. Nonetheless, the magnetic gripper, indigenously designed in the form of a rectangular paralleopiped, is definitely superior to the other viable alternatives for picking up bearing rings out of randomized heap. In fact, due to this randomized disposition of the bearing rings, we can't consider any standard robotic gripper that follows pick-and-place methodology. Since the exact location of the *object,* i.e. rings, cannot be specified in analytical term, all such grippers those perform well under structured layout will fail to work here.

Although vacuum gripper works satisfactorily under unstructured environment, but the major hindrance towards its performance is the size and weight of the object. These grippers are not suitable for our application, because of large size of the rings as well as their weights. In contrary, some other non-geometric design of the magnetic gripper would have been feasible alternative, if weight of the rings wouldn't be the bottleneck. For example, a shape-reconfigurable magnetic gripper, in the form of a long chain, may be thought of theoretically, but, the idea will also get discarded as the chain-gripper will be unable to pick large volume of rings, as required.

3.2. Design Schematics

The magnetic gripper has been designed as permanent magnet type with pneumatic pusher arrangement for the gripping actuation. The magnet is rectangular shaped having outside dimension 730 mm. x 375 mm. x 30 mm. Two separate permanent magnets are placed inside it, each of which consists of several *elemental magnets ("cells").* These elemental magnets have been arranged in a two-

[3] For example, in our application, there are four physical pillars, i.e. k=4, representing two edges of the *pentagon* and the rest three edges are represented by two open-ends, i.e. q=2.

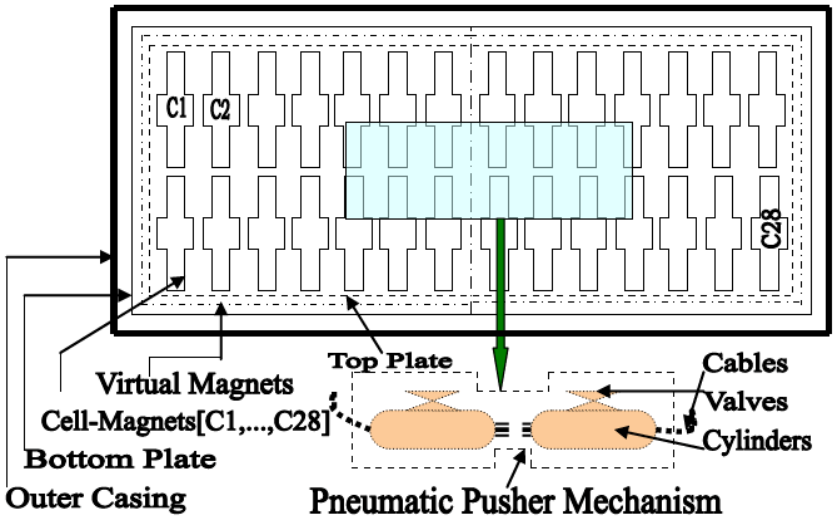

Figure 6: Internal Hardware of the Developed Magnetic Gripper.

dimensional array form and are supported by two plates, one from the top and the other from the bottom. The pneumatic pusher mechanism pushes these two magnets to establish contact with the bottom surface of the gripper, which by induction, gets magnetized and thereby becomes capable of gripping rings. Similarly, when the pusher goes up, detaching the contact with the bottom plate, the rings fall off immediately. This pusher mechanism is integrated with the gripper body, while the entire system has been fixed with the robot wrist by means of a special bracket-arm. The load cell is mounted between this bracket and the gripper body. The pusher mechanism is made operative through electrical relays and contacts, which also have necessary interfacing with the robot controller.

3.3. Fabrication

The process of fabricating the entire gripper begins with the realization of the *cell-magnets* and their disposition in a two-dimensional matrix (distributed under two larger magnets). The gripper is functionally divided in two parts, called, *virtual magnets*, each of which houses 14 nos. cell-magnets, in a 7 x 2 layout. Hence, in total, there are 28 cell-magnets in action. The cell-magnets have been designed with a customized shape, in order to attain maximum effectiveness towards gripping rings in a single pick. As the design inherits, the flat portion at the bottom of the gripper is getting magnetized with the help of these cell-magnets evenly. But, the cells have been attributed with a step-cut boundary (instead of simple rectangular shape) in order to have more magnetic induction effect at the side plates. Since the layout of the heap is randomized, all the three faces of the gripper, viz. bottom and two opposite sides must be utilized for picking up rings as best as possible. The pneumatic pusher mechanism is fabricated out of two cylinders, pushers, cable interlinks between the cylinders and outbound pneumatic lines. Figure **6** illustrates the internal layout and hardware of the developed magnetic gripper.

The actuation of the pusher mechanism is made operative through two types of sensors, viz. a] magnet power on/off sensor and b] pressure sensor. Magnet power on/off sensor detects for the availability of the electrical power to the gripper assembly for its operation (guided by the pusher sub-system). Once this sensor gives ok signal, the actuation of the pusher begins. On the other hand, the pressure sensor senses the operating pressure on the gripper plates (bottom and/or sides) and sends necessary signal to the robot controller in case of overloading. The overall actuation of the pusher system vis-à-vis magnetic gripper is shown schematically in Figure **7**.

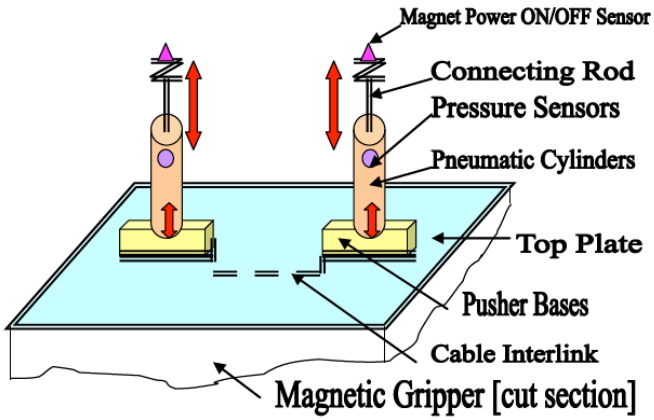

Figure 7: Schematics of the Magnetic Gripper Actuation.

It has been found from prolonged trials that the performance of the magnetic gripper degrades a lot due to the unevenness of the ring layers and haphazard way of placement with different orientations of rings. Besides, this random stacking of rings complicates the application program to a large extent. To tackle this problem, the gripper is provided with a pivot-type universal joint at the top in order to possess some compliance in its movements. Besides, in order to smoothen the magnetic grasp and to provide better tilt of the gripper over the heap, rubber padding is provided in between the pivot and the upper portion of the gripper body.

The rubber padding is registering omni-directional strain, which is translated in the form of angular tilt in the desired orientation. This has been proved very effective in better pick-up (of rings) by the gripper surfaces. The pivot assembly is in contact with the wrist and thereby, with the end of the robotic arm. Unlike the rubber padding, the pivot can have movements along X and Y directions only. These two degrees-of-freedom of the pivot will generate additional planar maneuverability of the gripper. Figure **8** illustrates the zoomed view of the pivot assembly. The photographic view of the final hardware of these design attributes is presented in Figure **9**.

3.3. Criticalities Involved in the Robotic Grasp

The complexity of the robotization process arises due to following reasons, namely, (a) size of the magnetic gripper, which is considerably large and non-compliant; (b) unstructuredness of the bearing rings; (c) uneven surface of the heap; (d) dynamic nature of the heap formation (after one lifting operation is over) and (e) structural hindrance offered by large-sized bins and/or baskets. Nonetheless, the major criticality of the system lies with the unstructuredness of the bearing rings inside the bin/basket. In a way, the problem

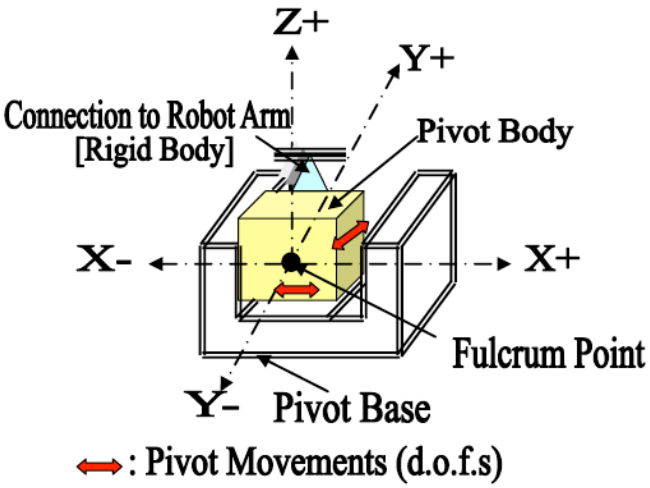

Figure 8: Manifestation of the Pivot Assembly.

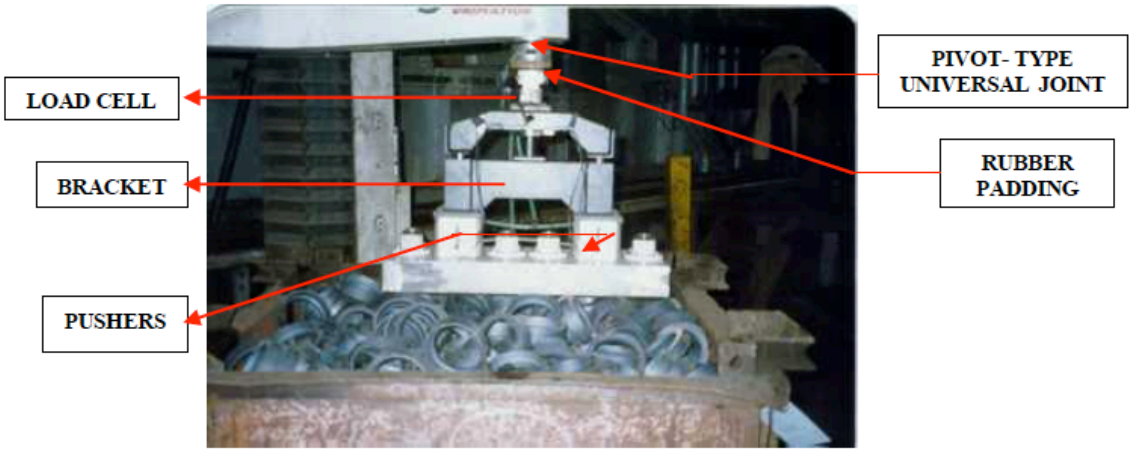

Figure 9: Photographic View of the Pivot-type Universal Joint and Rubber Padding.

encompasses *micro-motion planning* for the robot gripper in avoiding the edges and sharp corners of the large bins [40]. However, this random stacking of rings complicates the micro-motion planning, as the 'obstacle' geometry starts altering at each layer.

At a first glance to this application, planning a *safe* path in this workspace appears simple and subsequently, the robot program too. However, this inherent randomness in the system becomes instrumental in course of picking of rings in different operational cycles by the magnetic gripper, thereby letting the entire robotic process face substantial hindrances. These factors cumulatively become responsible for a loss in production time in the shop floor, affecting productivity. Nonetheless, the pivot and padding duple provides much better performance towards ring picking, as more number of *contact points* are generated on the surface of the magnetic gripper. Figure **10** describes the comparative effectiveness of the magnetic grasp, when rubber padding is used. It is apparent from the figure that we can differentiate the heap curvatures of the two cases analytically. Although both the equations, viz. C and C' are functions of same variables (x, y), where (x, y) signifies the location of ring at a particular time-instant, but their relationship functions (e.g. 'f' and 'g') are different.

3.4. Micro-motion Planning for the Magnetic Gripper

The global analysis of the grasp and the intended operation of material handling are carried out using *micro-motion planning* of the magnetic gripper. Algorithmic paradigm has been used for micro-level path planning of the magnetic gripper between the start and end locations in course of ring-handling operation, i.e. searching the 'best' alternative to avoid the collision with the heap. Figure **11** illustrates the above-mentioned facets in a schematic form.

Micro-motion planning of the magnetic gripper has been envisaged with respect to different attributes, namely, (i) modeling of the gripper for this specific

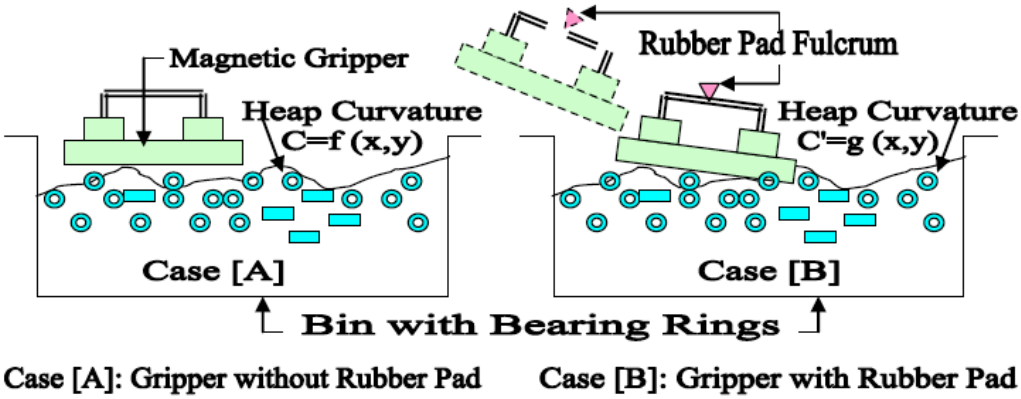

Figure 10: Comparative analysis of grasp of the magnetic gripper.

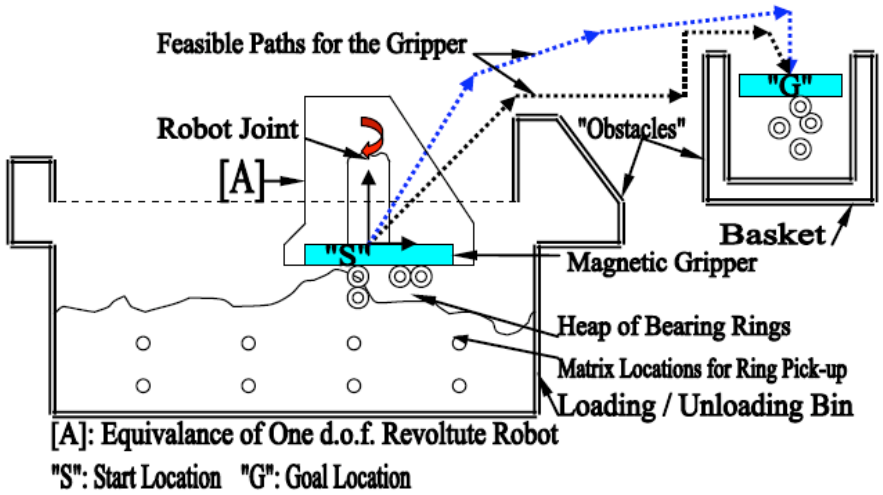

Figure 11: Schematics of the micro-motion path planning for the magnetic gripper.q0.

handling operation (through Finite Element Analysis of the magnetic gripper with regard to its load-carrying capacity and prediction of probable field-lines for stable gripping); (ii) modeling of the 'obstacle', i.e. corners and sharp edges of the loading and unloading bins; (iii) environment modeling, i.e. simplification of the 'real' objects (e.g. conveyor system, furnace, bins and baskets) to suitable layout in order to have less computational time for the overall system programming of the robot; (iv) discretization of the 3D space into suitable 'slices' and planning 'safe' path in two dimensions and finally (v) path planning in 3D space, corresponding to each robotic cycle.

The *micro-motion* of the magnetic gripper is kinematically equivalent to a *revolute robot* having one and half degree-of-freedom (refer Figures **9** and **11**). It may be noted that only the last link of the SCARA robot and the gripper are needed for computing this micro-motion path-points (from bin to basket). Thus, a *micro-robot* is being conceptualized having one revolute joint, one link, magnetic gripper unit and the small pivot-type universal joint between the link-end and the gripper. The revolute joint at the link will give rise to one d.o.f. and the rest will account for the pivot joint (kinematically which behaves like an approximate revolute joint).

The output of the various sensors, interfaced with the robotic system provide necessary input to the application program as well as evaluation of collision-free path layer-wise both individually and collectively. For example, the force sensor, in the form of a load cell, which is being used to sense the vertical force coming on the manipulator while the loading/ unloading of rings is in progress, provides necessary information about the selection of the 'start' (S) point for the 'best' path at every cycle. In other words, the start point (considered to be at the middle of the bottom surface of the magnetic gripper) will get shifted continuously in cases the gripper lifts rings weighing beyond the acceptable limit. In those situations, the gripper has to be re-positioned at different locations over the heap surface, thereby altering 'S'.

The environment of the robot has been modeled with exact dimensions of the system constituents (e.g. conveyor, bins, baskets, magnetic gripper etc.) for searching collision-free near-optimal path. The gripper, being of considerable size, has also been modeled as an *obstacle*, with the 'start' point embedded in it. The loading bin being large enough compared to the magnet, the gripper has been routed through 16 different locations, arranged in a 4 x 4 array, visiting the entire heap surface, dynamically generated for each layer after each pick. Obviously, the 2D mapping of the task-space at a particular location (out of these 16 positions) will differ from that of at some other location. Hence, the obstacle geometry (both in task-space and configuration space) has been considered separately for each such pick-up location and then the heuristic algorithm was treated. This procedure is repeated for each layer, until the magnet reaches the bottom of the bin / basket. However, during unloading operation, only one pick-up location has been used inside the basket, due to physical limitation of the basket size. Figure **12** shows the photographic view of the *micro-robot*, so formed, in course of ring-handling operation in the shop floor.

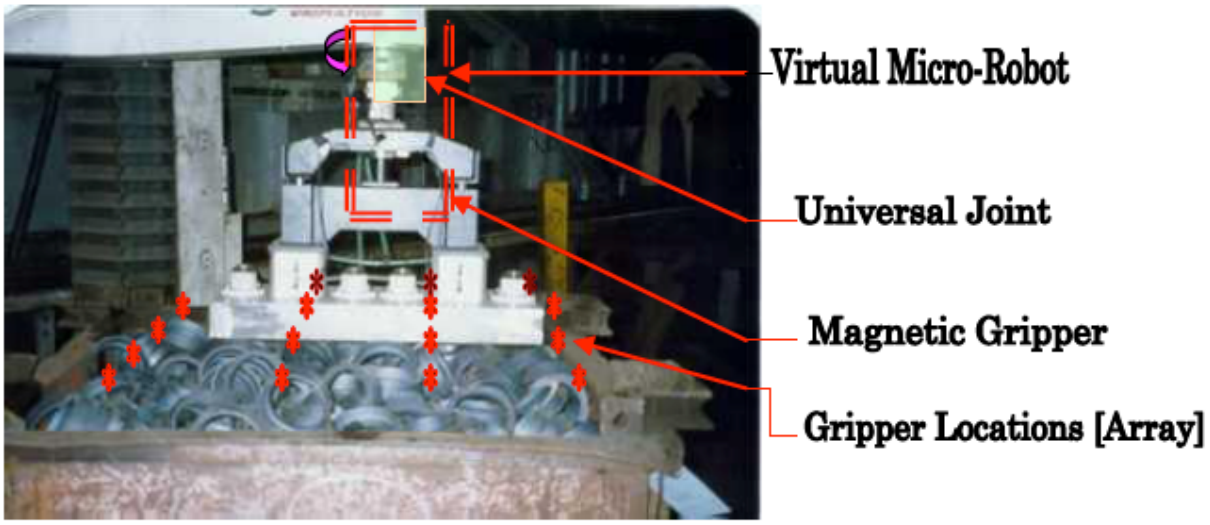

Figure 12: Photographic view of the action of the "Micro-robot".

Parameters like joint-speed, depth of travel, co-ordinated movement in X, Y or Z axes through 'safe nodes' (as reported by the algorithmic search) etc. have been specified in the main program as 'variables', so that those can be edited whenever required. The program also incorporates optimal search algorithm[4] to clear off rings from the corners of the bin and/or basket.

4. FINITE ELEMENT ANALYSIS OF THE MAGNETIC GRIPPER

The design and subsequent hardware manifestation of the prototype magnetic gripper was carried out using finite element – based models in *ANSYS 8.0*. In Finite Element Method (FEM), the magnet is conceptualized as an *assemblage* of sub-divisions (*elemental magnets*), connected through *nodes*. Since the actual variation of flux density inside the magnet-cells is unknown, its variation inside the *elements* is approximated in terms of a potential function using Maxwell's equations. The potential function is found out from a variational expression in terms of an energy-related function. The field region of the magnetic potential function is defined in terms of nodal values to obtain a solution of the magneto-static problem. However, the potential field solution is obtained from a set of finite element matrix equations. We will now describe various metrics of the FEA in detail, done in this case, in the following sub-sections.

4.1. Formulation of Finite Element Attributes

The FEA of the magnetic gripper system, i.e. gripper body, pivot mechanism and rubber padding has been governed by the following technical attributes, namely: [i] type of the magnetic element; [ii] optimal length of the magnetic flux; [iii] nature of rubber pad formation; [iv] alignment of the pivot; [v] cross-section and geometry of the cell-magnets; [vi] loading characteristics; [vii] pivot-pad dynamics and viii] vibration modes of the gripper system. Nonetheless, the analysis has been made considering a *Boolean model* of the gripper system assembly. In other words, we have assumed a-priori that the gripper system is composed of three member-units, which share some of the combined attributes, either separately or sub-assembly wise. These units are: [a] main body of the gripper, i.e. the *magnet*; [b] *pivot* and [c] *rubber pad*. It may be noted that the three main outcome attributes of the FEA in this case are: [a] magnetic analysis; [b] deformation and stress analysis and [c] vibration mode analysis.

4.2. Magnetic Analysis: Model and Results

Magnetic analysis was carried out on the *gripper body* using *ANSYS/Multiphysics*© module under *Windows*® platform. For the modeling, outside dimension of the magnetic gripper body was considered as (730 x 375 x 30) mm with upper and bottom plates, each of 3 mm thickness. The material for the bottom plate is taken as iron while we considered steel as the material for the rest of the structural components. The rectangular cell-magnets (refer Figure **6**), each having a dimension of (20 x 50 x 5) mm, are assumed to be sparse in a 5 x 3 rectangular array inside the gripper body. Although the FE model demands an accurate model of the physical prototype, a realistic compromise had to be ascertained in order to maintain simplicity and more importantly, linearity of the FEA results. For example, since we are concerned about the flux density and field intensity at the grasping part only in the present study, FE model too was generated for the grasp-zone of the magnetic gripper, i.e. the pivot and pusher mechanism were not modeled with their full kinematics. In fact, those two sub-assemblies were modeled as *static outgrowth*, added to the main body in Boolean fashion. *Solid 97* element[5] was used to mesh the entire solid model, thus generated. In the FE model, the permanent cell-magnets were *magnetized* in positive Z direction with $1x10^7$ N coercive force and naturally, the direction of polarization too was determined as the positive Z axis as the permanent magnet polarization direction corresponds to the co-ordinate signature of its elements. Nonetheless, we have used *Solid 97* element for this magneto-static analysis with three degrees-of-freedom per node, viz. the magnetic vector potentials, namely H_x, H_y and H_z.

Besides, in order to simulate real environment condition (i.e., air-gaps) an infinite boundary condition was applied around the gripper body using 8-node *Infin111* element. This element is suitable to model an open boundary of a 3D unbounded field problem, e.g. static magnetic field, wherein a single layer of these elements represent the external sub-domain of semi-infinite extent. It may be mentioned that because of

[4] The main application program for the robot was composed in VAL II. However, the optimal search algorithm was coded in C++ as a separate module.

[5] This 8-node 3D magnetic solid element models spatial magnetic fields with non-linear B-H and/or permanent magnet demagnetization curves.

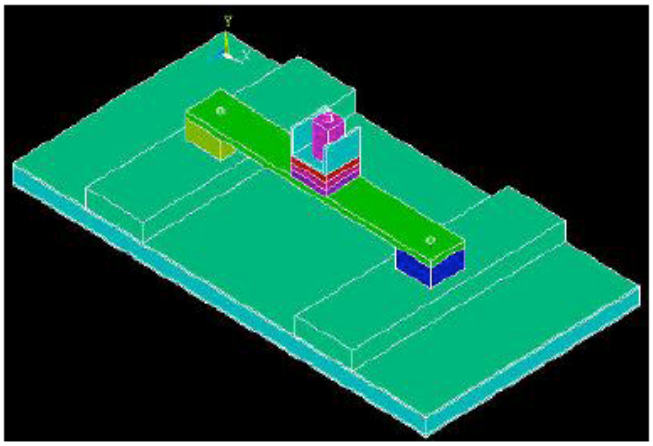

Figure 13: Boolean Model of the Magnetic Gripper System for FE Analysis.

using *Infin111* element at the boundary, we didn't need to apply any other boundary condition at the outer surface of the gripper body; the whole domain of the problem was extended to the infinity, by default. Figure **13** shows the complete FE model of the magnetic gripper system, with pivot (biased in Y-axis) and double layer rubber padding. Pivot mechanism was modeled as a small cube attached at a point with the rubber pad and both of these two sub-assemblies were modeled using *Solid 92* elements for FE meshing.

The auto-mesh generation of the above-mentioned FE model has been snap-shoted in Figure **14** below, wherein an inclined force was assumed to be in action on the bottom plate uniformly. This force is nothing but the *resultant force vector*, compounded by the reaction forces of the bearing rings in course of lifting.

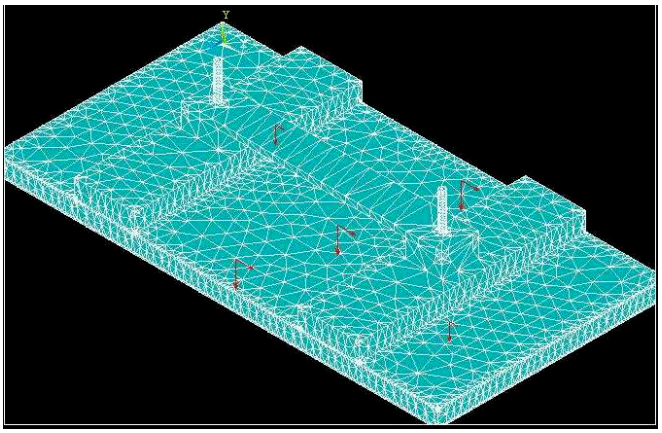

Figure 14: FE Mesh and Nodal Disposition of the Magnetic Gripper Activated Under Inclined Force.

With respect to the stipulated mesh, finally we have obtained the numerical value for the maximum field intensity (H) inside the grasp-zone of the magnetic gripper as 1030000 A/m[6] while the same for magnetic flux density (B) as 1.468 Tesla.

4.3. Deformation and Stress Analysis

Deformation and Stress analysis for the magnetic gripper assembly was carried out using *ANSYS/Mechanical*© module under *Windows*® platform. During the FEA, the upper part of the gripper body was kept stationary with zero degrees-of-freedom while the bottom plate was loaded with different types of forces. This external loading essentially simulates the combined reaction force from the bearing races (against the lifting pull by the gripper) and was grouped in three categories for this phase of FEA, namely, a] *point-edge* (*vertical* and *inclined*); b] *continuous* and c] *impulse*. However, the FE model excluded the *dynamics* of the pivot mechanism; rather, the pivot was conceptualized as a solid mass of mild steel having dimensions (30 x 30 x 50) mm. and while biasing, pivot was displaced by 10 mm. in X or Y axis. We have used 13N force in vertical direction as point-edge load while for simulating inclined force, additional 8N force was applied along horizontal direction. Likewise, in order to simulate continuous loading, uniform 12N/m^2 pressure was applied over the bottom plate of the gripper.

Although the analysis was straightforward for point-edge and/or continuous loading, it was quite different for impulse load. For simulating impulse loading and to maintain linearity, first we assumed some large force acting on the bottom plate and the mesh was analyzed with that force during the first time-instant. Later on, a very low value was assumed for the same force without altering the mesh or the boundary condition and FEA was performed for the second time-instant. In both the cases, stress/strain values were noted and the numerical difference in values, so obtained, gave an indication of the occurrence of the impulse force on the gripper body. It may be mentioned that in order to reduce computational time and complexity of the FEA, the central zone of the gripper was analyzed in depth because our initial experimentation with the prototype gripper revealed that the middle part of the gripper was susceptible to maximum variations in design parameters in contrast to sides. Table **1** presents the summary of the representative values for the maximum first principal stress and strain generated on the gripper body through FEA under various loading characteristics.

[6] This is the equivalent electro-magnetic field intensity, expressed in Ampere/meter [A/m].

Table 1: FEA Outcome for Stress and Strain for the Prototype Gripper under Different Loading Conditions

Force Type		Max. 1st. Principal	
		Stress [Pa]	Strain
Point-edge	Vertical	586326	0.450×10^{-5}
	Inclined	600139	0.278×0^{-5}
Continuous		339457	0.167×10^{-5}
Impulse		1140000	0.427×10^{-5}

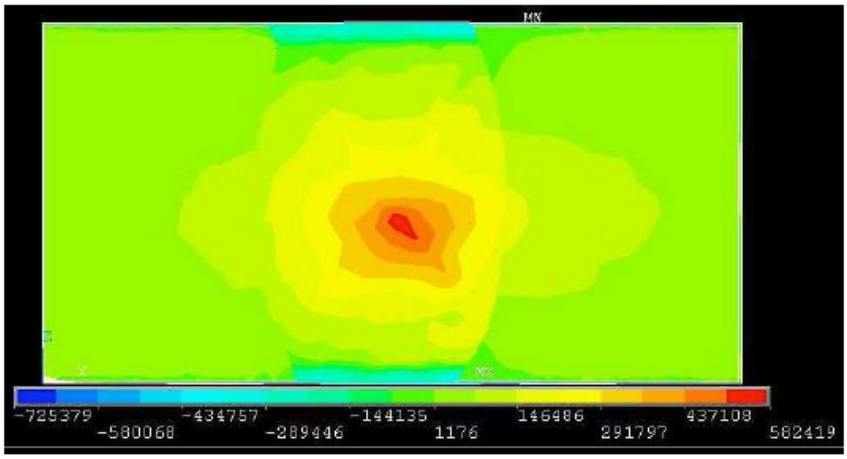

Figure 15: Variation of Principal Stress Along Z-axis on the Gripper Bottom Plate Under Impulse Load.

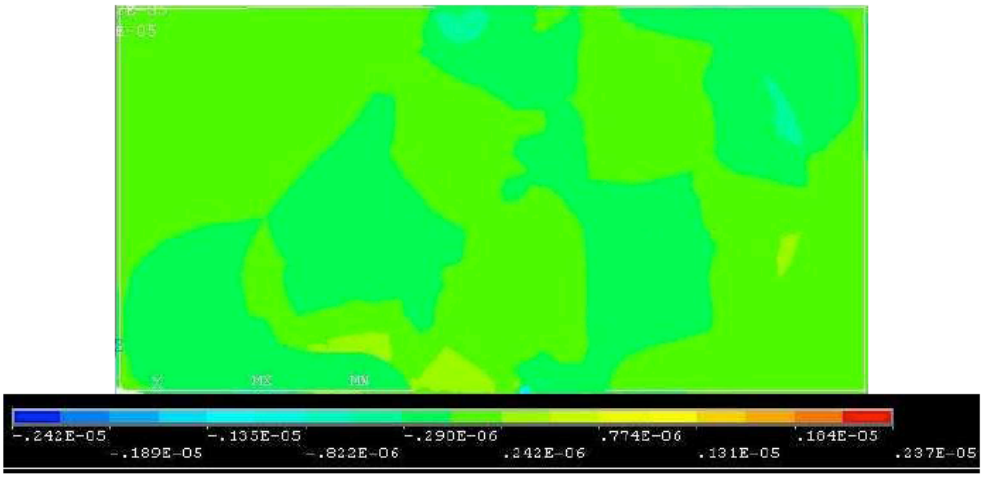

Figure 16: Variation of Shear Strain in XZ Plane at the Gripper Bottom Plate Under Impulse Loading.

Figure **15** shows the screenshot of the FEA wherein we obtained the variation of the principal stress (in Pa) on the bottom plate of the gripper along Z-axis under large impulse loading. And, the corresponding variation of shear strain in XZ plane on the gripper bottom plate under same impulse loading is presented in Figure **16**. Similar stress and strain contours were also generated while studying the effects with point-edge and continuous loadings. However, we are citing the contours against impulse loading only because of its severity of impact.

4.4. Vibration Mode Analysis

The prototype magnetic gripper system was simulated under vibration /modal analysis with the aid of *ANSYS/Mechanical*©. This analysis was carried out in two domains, namely when, a] *pivot and rubber pad*

were modeled as rigid unit (*Domain [a]*) and [b] *rubber pad was modeled with sufficient degrees-of-freedom* (*Domain [b]*). Neoprene and Mild Steel were considered for the modeling, respectively as the materials for rubber pad and pivot in both the cases. In *domain [a],* both pivot assembly and rubber pad were modeled as *solid* as well as *rigid* structure, attached to the main gripper body in Boolean fashion. In other words, pivot and rubber pad conjugate was assumed to be with zero degree-of-freedom, while the rest of the gripper assembly was free to move under external loading.

We have simulated a total of six interlinked scenarios in the joint pivot-rubber pad modeling, varying the layer of rubber pad as well as the biasing of the pivot assembly. The dimensions for the pivot assembly were taken as (30 x 30 x 50: length x breadth x height) mm in all simulation-runs, which is the actual physical size of the pivot assembly used in the prototype hardware. This size was arrived at after a few iterations, based on the space available between the end of the robot wrist and the load cell (attached to the magnetic gripper assembly). The actual space being too tiny, we do not have much leverage to alter the dimension of the pivot assembly. Hence, in all simulation runs, the dimension of the pivot assembly has been kept fixed. Likewise, the size of the rubber pad, having dimensions of (60x60x10: length x breadth x thickness) mm was also kept fixed, due to the limitation of the space, as stated above.

The first phase of the simulations were made with single layer rubber pad with three different biasing of the pivot, viz. [i] along X-axis; [ii] along Y-axis and [iii] in conjugate mode, i.e. biasing in the XY plane. With reference to Figure **8**, it is to be stated that the pivot body can have small movements along either X and Y axes or in XY plane; and the 'bias' is provided intentionally to ease the lifting capability of the gripper. The said bias is calculated as the small linear distance of shift along the axes/plane with respect to the fulcrum point (refer Figure **8**), i.e. the centroid of the pivot body. It is to be noted that close fit was to be ensured between the pivot base and the pivot body, otherwise the gripper system will be unstable. In such cases of instability, the grasp of the gripper per pick will be too less, making that particular run of the robotic cycle a waste. The 'bias' along X and Y-axes is physically realizable in the form of infinitesimal displacement along the desired axis, which, in simulation, was considered to be 0.8 mm. Likewise, the bias in XY plane is calculated as 0.7 mm (length of the diagonal of an infinitesimal square of side 0.5 mm, taken as the bias along X and Y axis).

The next phase of simulation was tried with similar set-up of pivot bias, but with double layered rubber pad. Although the betterment in grasp by using rubber padding is well-proven in the field-trials, the point which remained unresolved was about the overall thickness of such padding. On the other hand, we can't enhance the size and total thickness of the padding infinitely; because that will lead to hardware instability of the gripper system. Hence, as optimum choice, we have tried the simulation and performance through double layered rubber padding, having identical composition of layers.

However, we excluded the modeling intricacies due to the layout of cell-magnets while analyzing *domain [b],* thereby making the final model computationally simplified. The gripper body was modeled as one solid unit with effective density of the assembly to be equal to the density of the gripper with cell- magnets. The pivot mechanism was modeled as a small cube attached at a point with rubber pad and further hinged with the robotic arm. Like earlier FEAs, here too we used *solid 92* elements for the meshing. Table **2** highlights the summary of the FEA results obtained out

Table 2: FEA Results on Vibration Analysis of the Prototype Gripper System Under Two Domains

Rubber Pad Characteristics		Pivot Bias	Modal Frequency of Vibration [Hz.]		
			First Mode	Second Mode	Third Mode
Domain [a]	Rigid Body	Nil	41.64	50.782	99.449
Domain [b]	Single Layer	X-bias	4.061	5.872	9.135
		Y-bias	4.061	5.941	9.054
		Conjugate	4.024	5.542	9.013
	Double Layer	X-bias	2.916	4.074	6.340
		Y-bias	2.915	4.072	6.352
		Conjugate	2.574	3.786	5.859

of modal analysis of the prototype gripper system, actuated under these two domains.

It is observed from the results that while the effect of pivot biasing on the modal frequencies is negligible, double layer padding does affect the vibrational response significantly. In fact, rubber pad with double layer and pivot mechanism biased along conjugate plane becomes the optimal design combination for the gripper assembly in field conditions.

5. EXPERIMENTAL RESULTS

5.1. Logistics and Insight to System Metrics

The analysis of the gripping operation has been enumerated both by *localized perspective* and also in a *global* way. The performance of the gripper is analyzed and modeled with respect to its *lifting capacity* as well as *typical pattern* of the grasp, so formed. Field-trials were carried out with the robotic system in order to assess the performance capability in terms of object-lifting paradigms of the prototype gripper. This paradigm includes the following metrics, namely: [a] *payload lifted*, i.e. the gross weight of the rings picked up in a single cycle; [b] *cycle-time of operation*, i.e. the total time of flight for the gripper to run between loading and unloading stations; [c] *effect of power on position of the magnetic circuitry*, i.e. the gripper can be in action either when its body touches the ring-heap or when it starts approaching the heap; [d] *effect of side-collisions within the bin/basket* (more predominant inside the baskets during unloading operation) and [e] *effect of missed pick*, i.e. release of objects due to underweight pick (as it is not economical to run the full cycle with below-threshold marginal quantity of rings).

Among the said parameters, the two most significant determinants of the lifting efficiency of the gripper are: [i] the exact location for the *powering on* of the magnet circuitry and [ii] number of side-collisions inside bin/basket. We will now dwell on these two facets analytically.

5.1.1. Magnet power on position

The operation cycle of the robot must have requisite information a-priori whether the magnet is powered on amidst approaching the bin /basket or while touching the heap. In fact, in order to develop a successful off-line model of the grasping phenomena, we need to check for *missed picks*, besides the number of useful picks pertaining to lifting of rings from bin and/or basket. The *magnet power-on position* (mpp) does play an important role in analyzing the amount and nature of the missed picks and hence its modeling is crucial in overall analysis of the bin-picking operation in the shop-floor. Now, *mpp* can be at: [a] *on heap* (event 'a1') or [b] *during approach* (event 'a2'). Figure **17** explains the scenario and effect of magnet power on position over the payload of the gripper.

We consider the following probabilities, attached to the events 'a1' and 'a2', as mentioned above.

$$P(mpp = on \quad heap\big|_{'TRUE'}) \equiv P(a1) = p_1 \tag{26a}$$

$$P(mpp = during \quad approach\big|_{'TRUE'}) \equiv P(a2) = p_2 \tag{26b}$$

Here, the logical flag, "*TRUE*" means the event, which will lead to higher payload lift by the magnetic gripper, cumulated over all the cycles. That is to say, 'p_1' signifies the probability that the event 'a1' or "*mpp=on heap*" will lead to higher payload lift and similarly, 'p_2' symbolizes the same for the complimentary event 'a2' or "*mpp=during approach*". Although both 'a1' and 'a2' are equally likely events, it has been found from the trials that "*mpp=during*

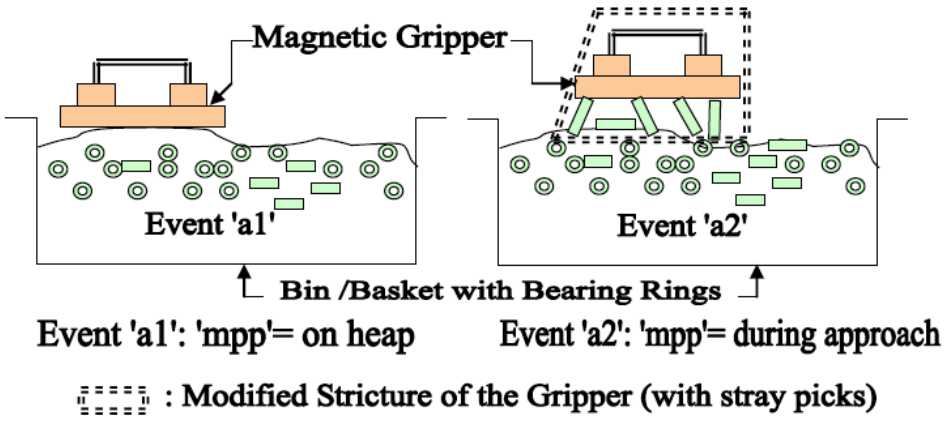

Figure 17: Comparative Scenario of Two Possible Locations of Magnet Power-on Position During Gripper Activation.

approach" is more probable to occur with better pick-up capability. Now, let us consider that the events 'a1' and 'a2' occur for 'q1' and 'q2' times respectively, within the total span of run-time of the robotic cycles. Therefore, for picking of rings from bin and basket, we get the conjugate probability for achieving better payload lift by the gripper as[7],

$$(p_1)^{q_1}(p_2)^{q_2} = k_{av} \tag{27}$$

Where, 'k_{av}' is a factor, dependent on various parameters related to gripping of rings, e.g. number of useful and missed picks, program and approach speed of the robot, run-time, total number of cycles etc. We will investigate this factor and related issues in the next sub-section. Now, since we experienced that $p_2 > p_1$, we can safely ascertain that $q_2 \geq q_1$, in order to increase /maximize 'k_{av}' and thereby the payload lifted. However, in order to solve for 'q_1' or 'q_2', we must get an expression for the ratio (q_1/q_2) as a function of 'p_1' and 'p_2'. Although (q_1/q_2) =1 is the ideal situation, where the operational cycles are equally divided between two events, 'a1' and 'a2', we can't adopt this model as the events are not equally probable. Thus, we have selected the ratio (q_1/q_2) to be equal to (p_1/p_2), because this ratio puts the bias $q_2 \geq q_1$ rationally in comparison to other two extremities, viz. $(p_1/p_2)^r$ and $(p_1/p_2)^{1/r}$,where 'r' is a positive numeral greater than 1. In fact, minimum increment of 'q_2' over 'q_1' (other than equality) is possible only when we have (q_1/q_2) = (p_1/p_2). Hence, we can evaluate 'q_1' using equation 27 with pre-assigned values for 'p_1' and 'p_2' as,

$$q_1 = \frac{\log(k_{av})}{\log(p_1) + \left(\frac{p_2}{p_1}\right)\log(p_2)} \tag{28}$$

Although it was observed from the trial runs that the event 'a2', i.e. "*mpp=during approach*" is more probable to occur with better pick-up capability it may not be advisable to use this position only for the initiation of activation. There is chance that the gripper may try to lift some irregularly placed rings, much ahead before reaching the actual heap, thereby causing jamming inside the bin and/or basket. This sort of unwanted phenomena may finally lead to low payload, despite powering on being done sufficiently earlier. And, obviously any kind of 'low lift' is not desired in the shop-floor, as it will effect in extra run-time and associated low throughput and loss in productivity. Hence both the positions for 'mpp' have got inherent advantage as well as bottleneck and an optimal compromise for availing the advantages of both of the possibilities has been used in equation 28.

5.1.2. Side Collisions

Collision between the gripper exteriors and the sides of the basket /bin is another important parameter that influences the overall payload lifted by the magnetic gripper. However, the effect of side collisions is more pronounced in case of unloading operation from the baskets. This is so because we have marginal clearance between the gripper and the side-surfaces of the basket and a slight undulation in the gripper will result in collision, which will finally end up in either very low payload lifts or sudden stoppage of the robotic system. Figure **18** explains the criticality of side collisions inside a basket.

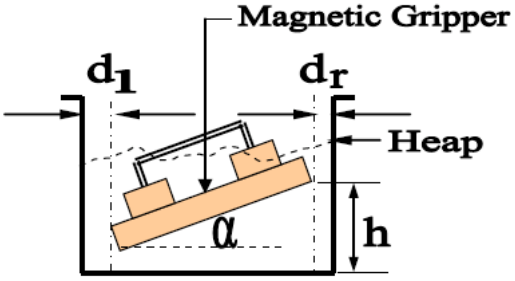

Figure 18: Schematic Showing the Occurrence of Side Collisions Inside a Basket.

As it is evident from Figure **18**, in an ideal condition, i.e. for no side collisions we must have $\alpha = 0^0$ and $d_l = d_r$. In the contrary, under a realistic situation side collision(s) is/are unavoidable and the number of side collisions (sc) will be function of side clearances and the absolute and angular position of the gripper. Mathematically we can state,

$$sc = fn\ (d_l, d_r, \alpha, h) \qquad and \quad W \propto \frac{1}{sc} \tag{29}$$

Where, 'W' is the payload lifted by the gripper.

5.2. Payload Lifted by the Gripper in Field: A Model

We shall emulate two different sub-models for estimating the payload lifted by the magnetic gripper in field, under the prevalent working environment. The first sub-model is to compute empirically the weight of the rings lifted by the gripper from the bin, while the second sub-model estimates the same during picking

[7] The probability of an event with repeated occurrence (say, 'n' times) is $(p)^n$, where 'p' is the element probability. In our case, 'n' signifies the number of robotic cycles, which may or may not be of equal duration.

of rings from the basket. The strategic parameters considered in the first sub-model are, [i] *missed pick*, [ii] *useful picks*, [iii] *robot speed* (VAL), [iv] *approach speed*, [v] *magnet power-on positions*, [vi] *run time* and [vii] *number of cycles*. The empirical model, in its generic form, for the case of picking rings from the bin is deduced as,

$$W_{bin} = \left[(x)^{mp} (y)^{up} (z)^{rs} (m)^{as} (p_1)^{q_1} (p_2)^{q_2} \right] (rt)(nc) \quad (30a)$$

Where, 'W_{bin}' is the weight of the rings lifted (in kg.) and the legends '*mp*', '*up*', '*rs*', '*as*', '*rt*' and '*nc*' signify missed pick, useful pick, robot speed, approach speed, run time and number of cycles respectively. The coefficients that need to be evaluated numerically, are 'x', 'y', 'z' and 'm'. We consider two groups of robot speed (as percentage of the machine speed in VAL), viz. 0.4 and 0.5 for the formulation. Likewise, two categories of approach speed were considered, viz. 0.8 and 0.9. The run-time is expressed in seconds. The parameters related to magnet power-on positions, viz. 'p_1', 'p_2', 'q_1' and 'q_2' have their usual significance as per equation 27.

From the analysis of the field-data on picking of rings from the bin, we finally derived the empirical model as,

$$W_{bin} = \begin{bmatrix} (1.0649)^{mp} (1.004)^{up} (5211.35)^{rs} \\ (4.0243)^{as} (p_1)^{q_1} (p_2)^{q_2} \end{bmatrix} (rt)(nc) \quad (30b)$$

The numerical value of 'k_{av}' for the case of picking of rings from bin is evaluated as 2.45968×10^{-5} (refer equation 27), which will be used in evaluating 'q_1 and 'q_2' by selecting the values for 'p_1' and 'p_2' a-priori.

Now, in case of second sub-model (i.e. for the basket), the parameters considered are, [i] *side collisions*, [ii] *missed pick*, [iii] *useful picks*, [iv] *robot speed* (VAL), [v] *magnet power-on positions*, [vi] *run time* and vii] *number of cycles*. The empirical model, in its generic form, for the case is deduced as,

$$W_{basket} = \left[(x)^{sc} (y)^{mp} (z)^{up} (m)^{rs} (p_1)^{q_1} (p_2)^{q_2} \right] (rt)(nc) \quad (31a)$$

Where, 'W_{basket}' is the weight of the rings lifted (in kg.) and the legends '*sc*', '*mp*', '*up*', '*rs*', '*rt*' and '*nc*' signify side collisions, missed pick, useful pick, robot speed, run time and number of cycles respectively. The coefficients that need to be evaluated numerically, are 'x', 'y', 'z' and 'm'. As in the case of bin, here also we consider two groups of robot speed (as percentage of the machine speed in VAL), viz. 0.4 and 0.5 for the formulation. Like the earlier model, the parameters 'p_1', 'p_2', 'q_1' and 'q_2' bear usual notation. We finally derived the empirical model on picking of rings from the basket as,

$$W_{basket} = \begin{bmatrix} (1.0014)^{sc} (0.968)^{mp} (1.024)^{up} \\ (1.108x10^{-5})^{rs} (p_1)^{q_1} (p_2)^{q_2} \end{bmatrix} (rt)(nc) \quad (31b)$$

The numerical value of 'k_{av}' for the case of picking of rings from basket is evaluated as 0.0719065, which is to be used in computing 'q_1 and 'q_2' by selecting the values for 'p_1' and 'p_2' beforehand.

5.3. Results From Field Trials and Analysis

We carried out field trials separately for loading and unloading cycles, in order to study the effect of inherent parameters on the final payload. For the loading cycle, data were taken with magnet powered ON when the gripper a] touched the heap of rings and b] approached the heap. Likewise for the unloading cycle, readings were noted, considering missed picks as well as number of side collisions, besides '*mpp*'. Table **3** and **4** present representative quantitative results, based on the regular robotic operation in the shop-floor.

An average weight of 7.054kg. per cycle was obtained during the loading process, which was adjudged satisfactory, considering the overall disposition of the magnetic gripper. However, unloading operation was more challenging technically due to problems like *missed picks* and *side collisions*. As a result, we found a drop in average pick-up during unloading, which is 4.91kg. Nonetheless, the gripper attained good dynamic compliance, while in operation, due to the presence of rubber padding. Besides effective contact with the heap surface, rubber padding has been proved useful at certain instances for operating the robot at higher speeds. In fact, the problem of *flying off* rings was observed at high speed operations, which was definitely a cause of concern because of potential health hazards to the operators and/or collision with other installations of the shop-floor.

However, the most interesting facet in these two sets of field results is the effect of 'mpp' on the overall payload lifted by the gripper. We have made a comparative analysis to pin-point this effect on the basis of available data and then postulated an ideal behaviour of the magnet power on position (*mpp*). Figure **19** presents the plot of the variation of payload

Table 3: Field Trial Results on Loading Cycle (From Bin to Basket)

Sl. No.	Total Cycle	Total Wt. (kg.)	Av. Wt. (Kg.)	Cycle Time (min: sec)	Magnet "Power ON" Location	Approach Speed[8]	VAL Speed
1	26	195.3	7.51	11:38	On heap	2.5	40
2	30	213.7	7.12	12:18	On heap	2.5	40
3	31	213.1	6.87	13:59	Approach	2.5	40
4	26	149.3	5.74	9:17	On heap	2.5	40
5	29	227.1	7.83	10:43	Approach	2.5	40
6	31	217.8	7.03	11:55	On heap	2.5	40
7	33	215.6	6.53	12:54	On heap	2.5	40
8	27	212.3	7.86	18:15	On heap	1.25	20
9	25	188.3	7.53	16s22	On heap	1.25	20
10	22	153.7	6.99	11:04	On heap	2.5	20
11	10	64.2	6.42	5:08	On heap	2.5	20
12	20	139.2	6.96	15:09	On heap	1.25	20
13	24	173.2	7.22	13:34	Approach	1.25	40
14	27	185.7	6.87	12:48	Approach	2.5	40
15	24	179.3	7.47	11:46	Approach	2.5	40
16	30	208.5	6.95	13:48	Approach	2.5	20
17	28	197.8	7.06	13:12	Approach	1.25	20
18	27	189.5	7.02	12:48	Approach	1.25	20
19	24	178.2	7.42	11:46	Approach	2.5	20
20	29	193.7	6.68	12:39	Approach	2.5	20

Table 4: Field Trial Results on Unloading Cycle (From Basket to Bin)

Sl. No.	Total Cycles	Total Wt. (kg.)	Average Wt. (Kg.)	Cycle Time (min: sec)	Magnet "Power ON" Location	Missing Pick (due to underweight)[9]	No. of Side Collisions[10]
1	42	195.8	4.66	22:54	Approach	0	0
2	33	233.1	7.06	22:26	Approach	5	0
3	41	172.7	4.21	20:18	Approach	3	2
4	44	174.1	3.96	22:41	On heap	3	20
5	40	176.6	4.41	21:44	On heap	9	0
6	37	186.3	5.03	21:23	On heap	8	0
7	45	163.8	3.64	23:53	On heap	15	1
8	56	185.7	3.31	29:35	On heap	17	6
9	43	198.6	4.62	24:36	On heap	8	5
10	33	212.6	6.44	21:12	On heap	7	3
11	39	224.7	5.76	22:45	Approach	2	0
12	40	179.5	4.49	20:36	Approach	0	1
13	43	183.7	4.27	22:23	Approach	0	0
14	37	185.3	5.01	21:56	Approach	0	0
15	32	193.8	6.05	22:08	Approach	2	2
16	41	201.4	4.91	23:12	Approach	3	0
17	40	209.7	5.24	20:41	Approach	0	1
18	38	202.5	5.33	21:28	On heap	8	3
19	36	187.8	5.22	22:28	On heap	9	6
20	41	190.8	4.65	21:37	On heap	5	7

[8] Representative speed of the gripper while approaching the heap of rings, coded in-line with VAL speed.
[9] It means that the gripper drops all the rings gripped, as the combined weight of the pick is less than the desired value (as coded in the program).
[10] It signifies the number of times the gripper hits the side-walls of the baskets, due to inaccessibility and hindrance in manoeuvrability inside the baskets.

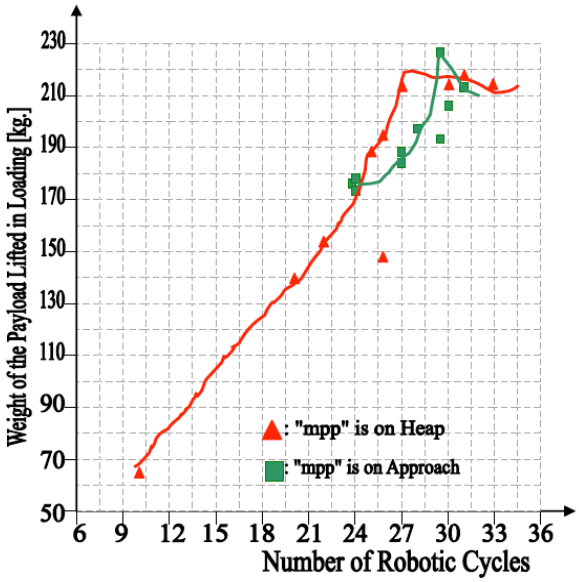

Figure 19: Variation of gripper payload during loading cycles against two different cases of 'mpp'.

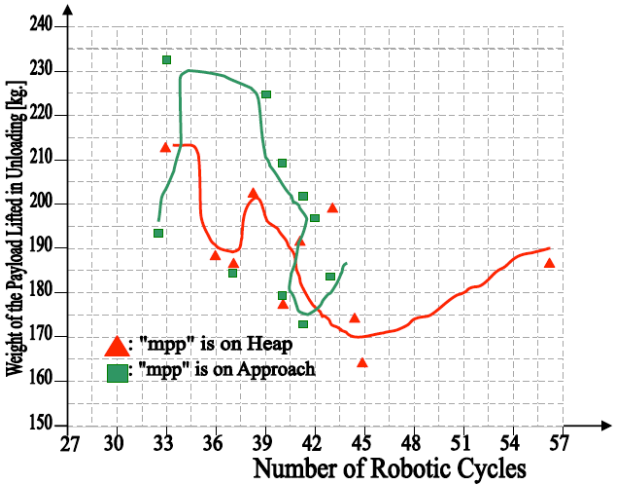

Figure 20: Variation of gripper payload during unloading cycles against two different cases of 'mpp'.

lifted during loading cycle against the number of robotic cycles, considering *mpp=on heap* and *mpp=on approach* separately. Likewise, the plot for the variation in weight of the gripper payload during unloading operation against the number of robotic cycles, considering the two cases of 'mpp' is illustrated in Figure **20**. For both the figures, *scatter diagram* points are highlighted with different colour legends for the two cases of '*mpp*' based on actual field-data points and mean curves were drawn thereon. It may be stated that these curves, corresponding to *mpp=on heap* and *mpp=on approach* are only representative and the actual curvature will very much depend upon the *sample-size*, like number of cycles and prevalent peripheral conditions at the shop-floor during the trial-runs[11]. However, we can adjudge the overall nature of the variation and that is the sole cause for this investigation. However, getting a trend equation for these plots is difficult, unless we take large number of data, i.e. large number of robotic cycles at a stretch.

Nonetheless, we can arrive at an ideal situation for these two cases of 'mpp', wherein a break-even may be evaluated in order to optimize the gripper payload, irrespective of the nature of robotic cycles. In other words, the postulation will be valid for both loading as well as unloading cycles, but the pre-condition for this

[11] Nonetheless, the parameters like *approach speed* and *delay* also affect the average lifting capacity.

optimization will be controlled by the occurrence of at least one *cross-over* between the two curves, i.e. mean-curves for '*mpp=on heap*' and '*mpp=on approach*'. In case of multiple cross-overs, we will consider the very first occurrence of it and the break-even point will be demarked accordingly. Based on the break-even point, we can switch between the two types of 'mpp's in order to optimize the weight of the payload lifted by the gripper in field. Figure **21** illustrates this postulation through a schematic plot.

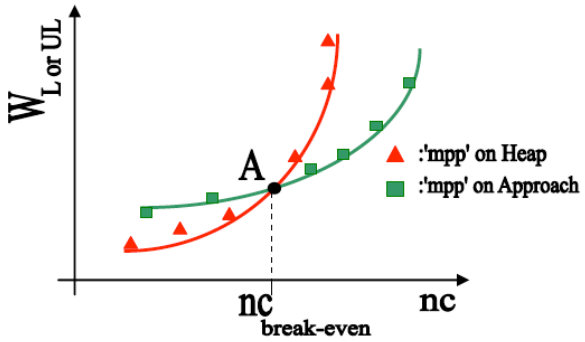

Figure 21: Strategy on 'mpp' For Optimized Payload Lift by the Gripper.

We can conclude from the field-data that, in general, loading cycles show better uniformity than unloading cycles and '*mpp = on approach*' is more coherent in disposition than the other alternative, i.e. '*mpp=on heap'*. Also, the pattern of variation of gripper payload during unloading cycles, as per Figures **19** and **20**, is more complex and probabilistic. Nonetheless, a saturation point is reached for both loading as well as unloading cycle, which may be acclaimed as the payload threshold of the gripper in field.

It is equally interesting to note the most likely ranges of lift (in kg.), as observed from typical loading cycles, activated during one full shift of operation of the annealing furnace. Figure **22** illustrates the result of the relevant analysis.

The actual field-data for the *frequency* of lift per shift against the *ranges*, as presented above, are 24, 27, 38, 42, 49, 50, 49, 41, 17, 13, 5, 5 and 1 respectively. Based on the test data (*sample*), statistical analysis has been made to compute sample mean and sample variance, which are 7.05 kg and 5.43 kg respectively. Since the sample size was considerably large, population variance was directly inferred from the sample data without much loss of accuracy. Hence the estimated values for Population Mean (μ) and Population Variance (σ^2) are 7.05 kg and 5.42 kg respectively.

6. CONCLUSIONS

The details of the development of a customized magnetic gripper intended for the material handling operation in the shop-floor have been delineated in the paper. The design is based on segregation of the magnetic field, by incorporating elemental magnets, placed in a two-dimensional array. This very design is the optimal choice for the robotic grasp for ferromagnetic objects under unstructured workspace. Random layout of the *objects* (i.e. bearing rings) is the nucleus of hindrance, which can be tackled best by our design of the gripper, with in-built compliance. The paradigms of *magnetic grasping* have been formulated based on the real-time study of the robotic system commissioned. Although the average lifting (of rings) by the gripper does vary due to many factors related to the random heap at the bins as well as at baskets, yet the overall grasp vis-à-vis performance of the gripper system has been found consistent and satisfactory.

ACKNOWLEDGEMENT

The author thanks the management of Tata Steel, Jamshedpur, India for partially financing this work, related to the commissioning of the robotic system in *field*. Special thanks and word of appreciation are due to Mr. Vivekanand, Mr. F. Mitra and Mr. D. Sengupta

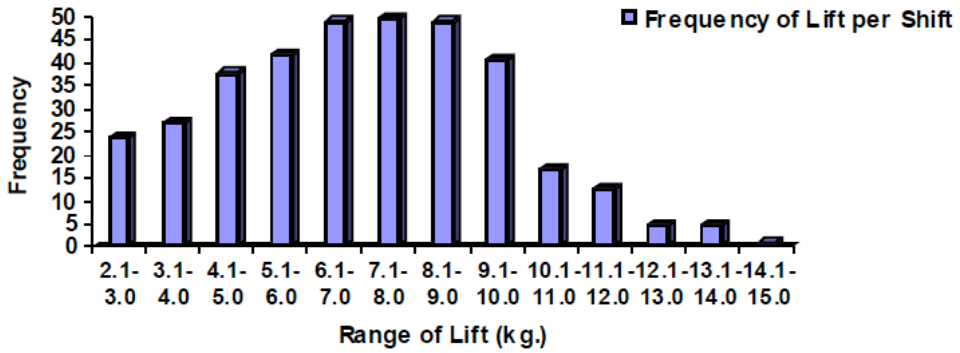

Figure 22: Statistical Analysis of the Payload Lift per Shift during Loading Cycles.

(from Automation Division, Tata Steel) for their encouragement and assistance. The co-ordination and help in programming the robot, rendered by the engineers of M/s Staubli Unimation, U.K. is acknowledged. The author also thanks Mr. Sumit Agarwal of Indian Institute of Technology, Kharagpur, India for carrying out the finite element based analysis on the magnetic gripper.

REFERENCES

[1] Adly AA, Mayergoyz ID, Gomez R and Burke ER. Computation of magnetic fields in hysteretic media. IEEE Trans Magn 1993; 29: 2380-2382. http://dx.doi.org/10.1109/20.281010

[2] Delta Torre Edward. A preisach Model For Accommodation. IEEE Trans Magn. Sept. 1994; 30(5): 2701-2707. http://dx.doi.org/10.1109/20.312509

[3] Chiampi M, Chiarabaglio D, Repetto M. A Jiles-Atherton and Fixed-Point Combined Technique For Time Periodic Magnetic Field Problems With Hysteresis. IEEE Trans Magn. Nov 1995; 31(6): 4306-4311. http://dx.doi.org/10.1109/20.488295

[4] Guarnieri M, Stella A, Trevison F. A Methodological Analysis of Different Formulations for Solving Inverse Electromagnetic Problems. IEEE Trans Magn 1990; 26(2): 622-625. http://dx.doi.org/10.1109/20.106394

[5] Dlala E, Saitz J and Arkkio A. Inverted and Forward Preisach Models For Numerical Analysis of Electromagnetic Field Problems. IEEE Trans Magn 2006; 42(8): 1963-1973. http://dx.doi.org/10.1109/TMAG.2006.877463

[6] Alotto PG, Girdinio P and Molfino P. A 2-D Finite Element Procedure For Magnetic Analysis Involving Non-linear and Hysteretic Materials. IEEE Trans Magn 1994; 30: 3379-3382. http://dx.doi.org/10.1109/20.312663

[7] Jiles DC and Atherton DL. Theory of ferromagnetic hysteresis. Journal of Magnetism and Magnetic Materials. 1986; 61: 48-60. http://dx.doi.org/10.1016/0304-8853(86)90066-1

[8] Papazov SP and Borshukova VD. Solution of Inverse Problems by Using FEM and Structural Functions. IEEE Trans Magn 1995; 31(6): 4297-4305. http://dx.doi.org/10.1109/20.488294

[9] Peng T, Gu CL, Rosseel K, Vanacken J and Herlach F. Advanced Numerical Simulation of Pulsed Magnets With a Finite Element Method. Measurement Science and Technology.2005; 16: 562-568. http://dx.doi.org/10.1088/0957-0233/16/2/032

[10] Caletka D, Deyhim A, Waterman D, Hunter-Dunn J and Blomqvist KI. FEA of Magnetic Loads on MAX II 46.6mm EPU Girders. Proceedings of the ninth International Conference on Synchrotron Radiation Instrumentation, Daegu, Exco, Korea 2006: 2; paper no. CP#010.

[11] Kildishev AV, Salon SJ, Chari MVK and Kwon OM. Spatial Harmonic Analysis of FEM Results in Mmagnetostatics. IEEE Trans Magn 2003; 39(5) Part 2: 3034-3036.

[12] Chiampi M, Negro A and Tartaglia M. A Finite-Element Method to Compute Three Dimensional Magnetic Field Distribution in Transformer Cores. IEEE Trans Magn 1980; 16: 1413-1419. http://dx.doi.org/10.1109/TMAG.1980.1060882

[13] Chiampi M, Chiarabaglio D and Repetto M. An Accurate Investigation on Numerical Methods for Non-linear Magnetic Field Problems. Journal of Magnetism and Magnetic Materials 1994; 133: 591-595. http://dx.doi.org/10.1016/0304-8853(94)90630-0

[14] Tsukerman I. Symbolic Algebra as a Tool For Understanding Edge Elements. IEEE Trans Magn 2003; 39(3): Part 1: 1111-1114.

[15] Tonti E. Finite Formulation of Electromagnetic Field. IEEE Trans Magn 2002; 38(2): Part 1: 333-336.

[16] Dittrich R, Schrefl T, Forster H, Suess D, Scholz W, Fidler J *et al*. Finite Element Simulation of Discrete Media With Granular Structure. IEEE Trans Magn 2002; 38(5): Part 1: 1967-1969.

[17] Jabbar MA, Zhejie Liu and Jing Dong. Time-stepping Finite-Element Analysis For the Dynamic Performance of a Permanent Magnet Synchronous Motor. IEEE Trans Magn 2003; 39(5): Part 2: 2621-2623.

[18] Simkin J and Trowbridge W. Optimization Problems in Electromagnetics. IEEE Trans Magn 1991; 27: 4016-4019. http://dx.doi.org/10.1109/20.104982

[19] Gottvald A, Preis K, Magele C, Biro O and Savini A. Global Optimization Methods for Computational Electromagnetics. IEEE Trans Magn1992; 28(2): 1537-1540. http://dx.doi.org/10.1109/20.123990

[20] Mifune T, Isozaki S, Iwashita T and Shimasaki M. Algebraic Multigrid Preconditioning For 3-D Magnetic Finite-Element Analyses Using Nodal Elements and Edge Elements. IEEE Trans Magn April 2006; 42(4): 635-638. http://dx.doi.org/10.1109/TMAG.2006.871617

[21] Liu Yuanqing and Yuan Jiansheng. A Finite Element Domain Decomposition Combined With Algebraic Multigrid Method For Large-Scale Electromagnetic Field Computation. IEEE Trans Magn. April 2006; 42(4): 655-658. http://dx.doi.org/10.1109/TMAG.2006.872464

[22] Vouvakis MN, Zhao Kezhong and Lee Jin-Fa. Finite-Element Analysis of Infinite Periodic Structures With Nonmatching Triangulations. IEEE Trans Magn 2006; 42(4): 691-694. http://dx.doi.org/10.1109/TMAG.2006.872483

[23] Trlep M, Hamler A, Jesenik M and Stumberger B. The FEM-BEM Analysis of Complex Grounding Systems. IEEE Trans Magn 2003; 39(3): Part 1: 1155-1158.

[24] Li Q and Lee KM. An Adaptive Meshless Method For Magnetic Field Computation. IEEE Trans Magn 2006; 42(8): 1996-2003. http://dx.doi.org/10.1109/TMAG.2006.876126

[25] Webb JP. An Estimator For Force Errors in Finite-Element Analysis. IEEE Trans Magn 2003; 39(3): Part 1: 1428-1431.

[26] Fu WN, Zhou P, Lin D, Stanton S and Cendes ZJ. Magnetic Force Computation in Permanent Magnets Using a Local Energy Coordinate Derivative Method. IEEE Trans Magn 2004; 40(2): 683-686. http://dx.doi.org/10.1109/TMAG.2004.824774

[27] Lee I and Goldwasser SM. A Distributed Test Bed For Active Sensory Processing. Proceedings of the IEEE International Conference on Robotics and Automation 1995; 925-930.

[28] Kirubarajan T, Wang H, Bar-Shalom Y and Pattipati KR. Efficient Multisensor Fusion Using Multidimensional Data Association. IEEE Trans Aerospace and Electronic Systems 2001; 37(2): 386-398. http://dx.doi.org/10.1109/7.937457

[29] Kalandros M and Pao LY. Covariance Control for Multisensor Systems. IEEE Trans Aerospace and Electronic Systems 2002; 38(4): 1138-1157. http://dx.doi.org/10.1109/TAES.2002.1145739

[30] Luo RC, Liu MH and Scherp RS. The Issues and Approaches of a Robot Multi-sensor Integration. Proceedings of the IEEE International Conference on Robotics and Automation 1987; 1941-1946.

[31] Thomopoulos SCA. Sensor Integration and Data Fusion. Journal of Robotic Systems 1990; 7(3): 337-372. http://dx.doi.org/10.1002/rob.4620070305

[32] Chen H, Kirubarajan T and Bar-Shalom Y. Performance Limits of Track-to-Track Fusion versus Centralized

Estimation: Theory and Application. IEEE Trans Aerospace and Electronic Systems 2003; 39(2): 386-400. http://dx.doi.org/10.1109/TAES.2003.1207252

[33] Chair Z and Varshney PK. Optimal Data Fusion in Multiple Sensor Detection Systems. IEEE Trans Aerospace and Electronic Systems 1986; AES-22(1): 98-101. http://dx.doi.org/10.1109/TAES.1986.310699

[34] Gan Q and Harris CJ. Comparison of Two Measurement Fusion Methods for Kalman-Filter-Based Multisensor Data Fusion. IEEE Trans Aerospace and Electronic Systems 2001; 37(1): 273-280. http://dx.doi.org/10.1109/7.913685

[35] Kaplan LM. Local Node Selection for Localization in a Distributed Sensor Network. IEEE Trans Aerospace and Electronic Systems. January 2006; 42(1): 136-146. http://dx.doi.org/10.1109/TAES.2006.1603410

[36] Roy D and Deb SR. A Stochastic Model and Performance Measure of a Multi-sensory System For Robotized Assembly Operation. Proceedings of the IEEE International Conference on Industrial Automation and Control India 1995: 285-290. http://dx.doi.org/10.1109/IACC.1995.465827

[37] Roy Debanik. A New Approach Towards Performance Measure of a Sensor-Augmented Remote Control System of Robots Aided by Stochastic Model. Proceedings of the International Conference on Knowledge Based Computer Systems ("KBCS-2000"), Mumbai India 2000; 517-528.

[38] Roy Debanik. Modelling and Development of a Sensor-integrated Industrial Robotic System For Handling Steel Bearing Races in an Unstructured Environment. Proceedings of the 17th. All India Manufacturing Technology, Design and Research Conference, Warangal, India 1997; 229-235.

[39] Roy D. Development of a Sensor-augmented Industrial Robotic System For Handling Steel Bearing Races in an Unstructured Environment. Journal of Intelligent and Robotic Systems 2005; 43(1): 55-76. http://dx.doi.org/10.1007/s10846-005-2963-9

[40] Roy D. On The Algorithmic Path Planning of Industrial Robots in a Cluttered Spatial Manifold: A Case Study Using Visibility Map Paradigms. Proceedings of the International Conference on Knowledge Based Computer Systems ("KBCS-2000"), Mumbai, India 2000: 529-541.

Received on 13-06-2015 Accepted on 24-07-2015 Published on 31-07-2015

DOI: http://dx.doi.org/10.15377/2409-9694.2015.02.01.1